Computational and Structural Biotechnology Journal 21 (2023) 3355–3368

Contents lists available at ScienceDirect

Computational and Structural Biotechnology Journal

journal homepage: www.elsevier.com/locate/csbj

Research article

Theoretical and experimental studies on the interaction of biphenyl ligands with human and murine PD-L1: Up-to-date clues for drug design

Greta Donati [a,1], Vincenzo Maria D'Amore [a,1], Pasquale Russomanno [a], Linda Cerofolini [b], Jussara Amato [a], Simona Marzano [a], Maria Salobehaj [b], Domenico Rizzo [b], Giulia Assoni [c,d], Alfonso Carotenuto [a], Valeria La Pietra [a], Daniela Arosio [e], Pierfausto Seneci [d], Marco Fragai [b], Diego Brancaccio [a,*], Francesco Saverio Di Leva [a,*], Luciana Marinelli [a,*]

[a] Department of Pharmacy, University of Naples Federico II, Via D. Montesano 49, 80131 Naples, Italy
[b] Magnetic Resonance Center and Department of Chemistry, University of Florence and Interuniversity Consortium for Magnetic Resonance of Metalloproteins (CIRMMP), Via L. Sacconi 6, 50019 Sesto Fiorentino, Italy
[c] Department of Cellular, Computational and Integrative Biology (CIBIO), University of Trento, Via Sommarive 9, Povo I-38123, Trento, Italy
[d] Department of Chemistry, University of Milan, Via C. Golgi 19, 20133 Milan, Italy
[e] Istituto di Scienze e Tecnologie Chimiche "Giulio Natta" (SCITEC), Consiglio Nazionale delle Ricerche (CNR), Via C. Golgi 19, Milan 20133, Italy

ARTICLE INFO

Article history:
Received 4 April 2023
Received in revised form 7 June 2023
Accepted 7 June 2023
Available online 8 June 2023

Keywords:
Immunotherapy
Cancer
Programmed Death Ligand 1
Computational Chemistry
Drug Design

ABSTRACT

Today it is widely recognized that the PD-1/PD-L1 axis plays a fundamental role in escaping the immune system in cancers, so that anti-PD-1/PD-L1 antibodies have been evaluated for their antitumor properties in more than 1000 clinical trials. As a result, some of them have entered the market revolutionizing the treatment landscape of specific cancer types. Nonetheless, a new era based on the development of small molecules as anti PD-L1 drugs has begun. There are, however, some limitations to advancing these compounds into clinical stages including the possible difficulty in counteracting the PD-1/PD-L1 interaction in vivo, the discrepancy between the in vitro IC_{50} (HTFR assay) and cellular EC_{50} (immune checkpoint blockade co-culture assay), and the differences in ligands' affinity between human and murine PD-L1, which can affect their preclinical evaluation. Here, an extensive theoretical study, assisted by MicroScale Thermophoresis binding assays and NMR experiments, was performed to provide an atomistic picture of the binding event of three representative biphenyl-based compounds in both human and murine PD-L1. Structural determinants of the species' specificity were unraveled, providing unprecedented details useful for the design of next generation anti-PD-L1 molecules.

1. Introduction

In recent years, immunotherapy has emerged as a powerful strategy for cancer treatment so that, in 2018, the Nobel Prize in Physiology or Medicine was awarded to Allison and Honjo "for their discovery of cancer therapy by inhibition of negative immune regulation" [1]. Currently marketed immunotherapeutic drugs are monoclonal antibodies (mAbs) that interfere with specific modulatory systems, called immune checkpoints, acting at the interface between tumor and immune system cells, particularly T-lymphocytes (T cells) [2]. Immune checkpoint receptors (ICRs) are constitutively expressed on the surface of T cells to tackle overactive adaptive responses to self-antigens, thus preventing autoimmune reactions.[3,4] On the other hand, the overexpression of their ligands on cancer cells allows the tumor to evade the immune surveillance [5,6]. Among the immune checkpoints, the programmed cell death protein 1 (PD-1, also known as CD279) and its ligand programmed death ligand 1 (PD-L1, also known as CD274 or B7-H1) [7,8] play a

Abbreviations: BMS, Bristol Myers Squibb; ESP, electrostatic potential; GAFF, Generalized Amber Force Field; HTRF, homogeneous time resolved fluorescence; ICR, immune checkpoint receptor; mAb, NSCLC, monoclonal antibodynon-small cell lung carcinoma; PD-1, programmed cell death protein 1; PD-L1, programmed death ligand 1; RMSF, root mean square fluctuation; SPME, smooth Particle-Mesh Ewald; SPR, surface plasmon resonance; RESP, restrained electrostatic potential

* Corresponding authors.
E-mail addresses: diego.brancaccio@unina.it (D. Brancaccio), francesco.dileva@unina.it (F.S. Di Leva), lmarinel@unina.it (L. Marinelli).

[1] These authors contributed equally.

https://doi.org/10.1016/j.csbj.2023.06.006

major role in the T-cells exhaustion in many cancer types including melanoma, breast, pancreatic, renal and non-small cell lung (NSCLC) carcinomas [9–11]. More than 1000 clinical trials have evaluated the antitumor properties of anti-PD-1/anti-PD-L1 mAbs. As a result, some anti-PD-1 (e.g. nivolumab and pembrolizumab) and anti-PD-L1 (e.g. atezolizumab, avelumab and durvalumab) mAbs have entered the market, revolutionizing the treatment landscape of the above mentioned tumors [12–17]. Notably, the number of approved mAbs is constantly growing, including agents which are effective towards further malignancies. With the aim to overcome the limitations of mAbs (e.g. high production costs and side effects), while improving the patient's compliance (e.g. oral administration), macrocyclic peptides, peptidomimetics and non-peptidic small molecules are currently being developed as anti-PD-L1 agents, opening a new era for drug discovery in immunotherapy [18–39]. Particularly, the biphenyl-based anti-PD-L1 agents, originally discovered by Bristol Myers Squibb (BMS), have been proven successful in disrupting the PD-1/PD-L1 interaction in vitro through a protein dimerization mechanism [18–28]. The huge efforts spent on biphenyl-containing molecules have resulted in an impressive number of publications and patents, especially in the last few years [18–28]. However, the clinical development of anti-PD-L1 small molecules is still in its infancy; in fact, there is only one small organic molecule, INCB086550, which is currently in Phase II clinical trials [40,41]. Limitations to advancing small molecule candidates is due to many factors, including: i) the possible difficulty in counteracting the PD-1/PD-L1 interaction in vivo; ii) the absence, at least in the PD-L1 monomeric form, of a well-defined ligand pocket; iii) the discrepancy between in vitro IC_{50}s, typically obtained through homogeneous time resolved fluorescence (HTRF) assays on the human dimer PD-1/PD-L1, and cellular EC_{50}s derived from immune checkpoint blockade co-culture assay [2]; and iv) unexpected differences in the ligands' affinity between human and murine PD-L1, which can affect preclinical evaluation. In fact, in spite of the high structural similarity between human and murine PD-L1 (87.6%, Ig-like V-type domain: 19–127 amino acids), the ligand binding affinity towards these targets can considerably vary depending on the examined small molecule [2,24,25,42,43]. In this scenario, an analysis of the binding to mPD-L1 should be preliminarily done for any lead ligand before selecting the proper mouse model [21]. In case the ligand shows affinity for mPD-L1, syngeneic animals, expressing both the murine ligand and receptor, can be employed [44,45]. Alternatively, mouse knock-in models able to express human PD-1 (i.e. humanized animals) have to be used. Certainly, to speed up preclinical development and to reduce the mouse model complexity, the design/development of small molecules active on both species would be highly desirable. However, the structural basis of their human vs murine PD-L1 activity and selectivity is only partially known. To this regard, based on a sequence alignment and X-ray complexes analysis, it has been recently suggested that the species' specificity of the BMS small molecules may mainly reside in the Met115/Ile115 substitution that would hamper their biphenyl moiety to properly allocate in the mPD-L1 pocket [25]. In this complex picture, there is an urgent need to move toward a next generation of anti-PD-L1 small molecules, possibly endowed with a high residence time in both hPD-L1 and mPD-L1, which should, in turn, increase protein dimer stabilization that is necessary to achieve potent in vivo activity. To this regard, the existence of some X-ray structures of hPD-L1 complexed with structurally diverse biphenyl-based compounds (BMS-202 [19], BMS-1166 [26], LH1307 [22]) or cyclic peptides furnishes precious knowledge, even with the limits of a static view that neglects the ensemble of interchangeable protein states that exists with or without a specific bound ligand.

Herein, a combined experimental and computational approach was used to add another piece to the puzzle of the ligand-PD-L1 binding event, and to the species' specificity determinants. To accomplish the latter aim, we selected three diverse biphenyl-based compounds: the reference ligand BMS-202 [18] (high affinity for hPD-L1 but complete loss of affinity for mPD-L1), P18 [32] (high affinity for both h- and mPD-L1) and our triazine-based RS39 [33] (higher affinity for hPD-L1 than for mPD-L1) (Fig. 1). We first characterized their equilibrium dissociation constants for both the human and the murine orthologues through Microscale Thermophoresis (MST) assays, and then investigated their binding poses using Nuclear Magnetic Resonance (NMR) and extensive molecular dynamics (MD) simulations to characterize the conformational landscape of the binding domain of hPD-L1. Our study delivers unprecedented details on the dynamics of the interaction between small molecule ligands and both human and murine PD-L1. Finally, a comparison with other biphenyl ligands provides clues to design a new generation of smart molecules endowed with possibly increased residence time in PD-L1 and capability to stabilize its homodimer formation.

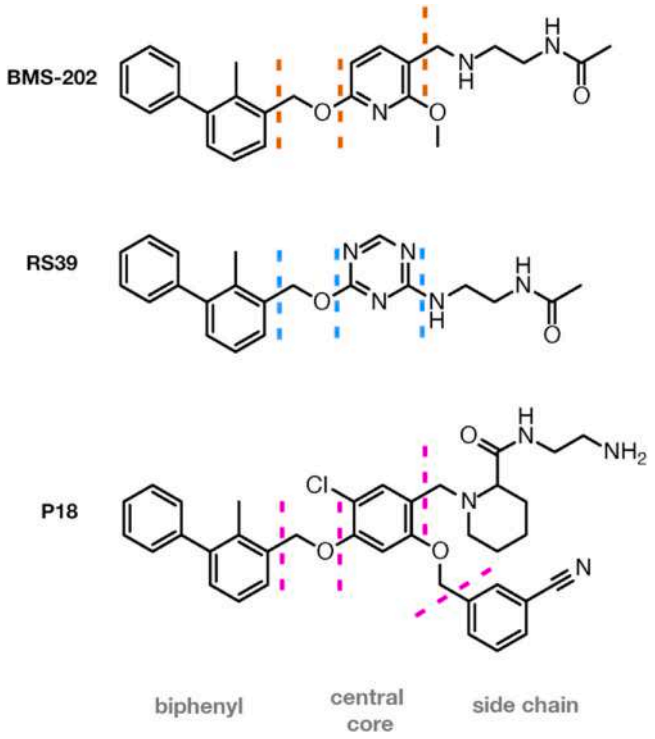

Fig. 1. Chemical structure of the investigated biphenyl-based PD-L1 inhibitors. The main specific functional groups of each inhibitor are highlighted by colored dashed lines.

2. Materials and methods

BMS-202 and P18 were purchased as pure substances from Selleck Chemicals LCC and InvivoChem LLC, respectively, while RS39 was synthesized according to our previously published procedure [33]. All compounds were > 95% pure by HPLC analysis. Human PD-L1 protein was expressed and purified as previously described [33], while murine PD-L1 protein was purchased from Abcam PLC.

2.1. MicroScale thermophoresis (MST) binding assay

MST is a rapid and easy methodology to quantify interactions between small molecules and (bio)macromolecules in solution. The principle of the technique is based on the thermophoresis, i.e., the movement of a fluorescently labelled target molecule under microscopic temperature gradients. The thermophoretic movement is determined by the size, charge, and hydration shell around the

molecule. As the interaction of a ligand to the target molecule changes at least one of these parameters, it also alters the thermophoretic movement of the molecule. This effect can be used to evaluate the dissociation constant, K_D. For this purpose, unmodified PD-L1 proteins (human and murine) were labelled using the Monolith RED-NHS Kit (NanoTemper Technologies, Germany) following the standard protocol. This labeling kit was already employed by Magiera-Mularz et al. [25] and Sun et al. [46] for labeling the PD-L1 protein in MST experiments. The dye carries a reactive NHS-ester group that reacts with primary amines of lysine residues to form a covalent bond. Measurements were performed on a NanoTemper Monolith NT.115 instrument (NanoTemper Technologies, Germany). For all binding experiments, the labelled PD-L1 proteins were used in a concentration of 100 nM in 10 mM Tris (pH 8.0), 20 mM NaCl buffer. Compounds were first dissolved at a concentration of 8 and 20 mM in pure DMSO, then diluted to 0.8 or 2 mM using the same buffer of the protein. Serial dilutions of the compounds (1:2 from 0.8 or 2 mM solution) in 10 mM Tris (pH 8.0), 20 mM NaCl buffer containing 10% DMSO were made, and 10 μL of each dilution was mixed with 10 μL of labelled protein in buffer only, aiming for the final DMSO concentration of 5% in each sample. This percentage of DMSO was already used by Ganesan et al.[1] to assess the binding affinity of other BMS derivatives toward hPD-L1 by MST. However, to exclude interferences of DMSO in protein stability, we acquired 1D ^{1}H NMR spectra of hPD-L1 in the same buffer used for MST measurements (i.e., 10 mM Tris, pH 8.0, 20 mM NaCl, 5% DMSO). No changes in the protein folding were detected (Supplementary Fig. S1), suggesting that 5% DMSO did not affect hPD-L1 stability. Samples were then loaded into Monolith Standard Treated Capillaries (NanoTemper Technologies, Germany). Measurements were run and analyzed as previously reported [47].

2.2. Nuclear magnetic resonance experiments

All the NMR spectra were acquired at 298 K on Bruker NMR AVANCEIII HD and AVANCE NEO NMR spectrometers operating at 950, 900 and 600 MHz, ^{1}H Larmor frequency, and equipped with cryogenically cooled probes. The spectra were processed with the Bruker TOPSPIN software packages and analyzed by the program Computer Aided Resonance Assignment (ETH Zurich; Keller, 2004). The protein assignment was based on the data reported in the Biological Magnetic Resonance Data Bank under the accession code 51169 [17].

For the NMR studies, the ^{15}N-isotopically enriched protein, at the concentration of 50 μM, was dissolved in 540 μL of buffer (10 mM Tris at pH 8, 20 mM NaCl, proteases inhibitors, 0.1% NaN_3) and 60 μL of ^2H_2O. The binding behavior of the ligands (BMS-202, RS39 and P18) on PD-L1 protein have been investigated by monitoring the changes in cross-peak intensity ratio (I/I_0) occurring in the 2D ^{1}H–^{15}N HSQC spectrum of the protein upon the addition of increasing amounts of the ligands, solubilized in DMSO-d_6, to reach concentrations of 6.25, 12.5, 18.75, 25, 50 μM.

For the protein stability analysis in DMSO, 1D ^{1}H NMR spectra of hPD-L1 (50 μM) were acquired in presence and absence of 5% of DMSO-d_6. The spectra were obtained using 512 scans per spectrum with a recovery delay of 1.5 s.

2.3. Computational methods and procedures

2.3.1. Preparation of the hPD-L1 complexes

The crystallographic hPD-L1/BMS-202 complex was retrieved from the Protein Data Bank (PDB code: 5J89 [19]). After its preparation, this structure was employed to perform molecular docking simulations on RS39 and then submitted to MD simulation (see next Sections). To carry out docking calculations on P18, we instead selected the crystallographic structure of hPD-L1 co-crystallized with BMS-1166 (PDB code: 6R3K [26]). This choice was based on the structural and hindrance similarity between BMS-202 and RS39 and between BMS-1166 and P18, respectively. In both the selected structures, the protein is in a homodimeric form with the small organic inhibitor at the interface of the two chains. Our 2D ^{1}H–^{15}N HSQC experiments also suggested that RS39 and P18 can bind at the interface of two PD-L1 molecules, similar to BMS-202. Further evidences of the homodimer formation when PD-L1 binds small organic molecules corroborated our decision [18–23,26,48–52]. For these reasons, hPD-L1 (or murine PD-L1) is here always referred as to the protein homodimer.

The hPD-L1 structure co-crystallized with LH1307, a C_2-Symmetric ligand (PDB code: 6RPG) [22], was employed for molecular docking simulations on INCB086550 [38], GS-4224 [39], BMS-40770 [53] and BMS-1058 [54]. Also the most representative conformations extracted from the MD simulation (see the procedure described in Paragraph 2.3.4) on the hPD-L1/BMS-202 complex (displaying the highest flexibility in the binding site over the simulated time scale - see next paragraphs), were used for docking of INCB086550 [38], and GS-4224 [39].

All the PDB structures were prepared by employing the graphical interface of the Schrödinger's molecular modelling platform, Maestro [55] v. 12.7.156. In detail, the proteins were prepared with Protein Preparation Wizard [56], included in Maestro. Hydrogen atoms were added and missing side chains were filled in by using the Prime [57–59] module, while crystallographic water molecules were deleted. The N-terminal and C-terminal residues were capped with the acetyl and N-methyl amide groups, respectively. To properly describe the protonation state of the protein residues and to also describe the hydrogen bonding networks correctly at neutral pH, the protonation states were assigned evaluating their pK_a with the Propka [60] program included in Maestro. Finally, a relaxation procedure was performed by running a restrained minimization only on the initially added hydrogen atoms according to the OPLS2005 [61] force field.

All the ligands were built and prepared through the LigPrep [62] module of Maestro, employing the OPLS2005 force field. Epik [63–65] was used to evaluate the compounds' pKa at neutral pH and so to properly describe their protonation state. The ligands were then optimized at molecular mechanics level through the MacroModel [66] program included in the Schrödinger suite of programs.

2.3.2. Molecular docking simulations

First, receptor grids of 30 Å × 30 Å × 30 Å were computed for the 5J89, 6R3K or 6RPG structures around the centroids of the co-crystallized ligands, BMS-202, BMS-1166 or LH1307, respectively, since it was reasonable to assume that the compounds docked in such structures could bind to the same pocket. During the grid calculation, the co-crystallized ligand was deleted from the respective 3D structure. Docking simulations were performed by using the Glide SP [67–70] software included in Maestro using default parameters. Sampling of nitrogen atoms inversions (when not belonging to cycles) and of different rings conformations were allowed, while non-planar amide conformations were penalized. In all the simulations the receptor was kept fixed, while the ligand was treated as flexible.

In all cases, docking converged to a well-defined binding mode; indeed, an almost complete overlap of the ligand was possible for the best 20 predicted poses. For P18, the lowest energy pose was chosen as starting point for molecular dynamics simulations, while for RS39, we selected the pose with linear side chain that seemed to maximize its interactions with the protein.

2.3.3. Preparation of the mPD-L1 complexes

The crystallographic structure of apo murine PD-L1 was retrieved from the Protein Data Bank (PDB code: 6SRU) [25]. Experimental (also from this work) and computational evidences show that

organic small molecules favor the formation of PD-L1 homodimer. Moreover, in the hPD-L1 case, these ligands establish interactions with part of the residues (given the smaller size of the inhibitors) involved in the hPD-1/hPD-L1 complex [71]. Thus, it was reasonable to assume that the investigated inhibitors could bind to mPD-L1 in the same region as in hPD-L1, thereby inducing the homodimerization of the murine receptor. For both RS39 and P18, a mPD-L1/ligand trimeric complex was thus built by overlapping the protein monomer to each of the two hPD-L1 chains in the respective docking complexes with human protein. Conversely, no trimeric complex was generated for BMS-202 since it is known that this compound does not bind mPD-L1 [25].

The obtained mPD-L1 dimers were subjected to the same protein preparation of hPD-L1 described in the previous Section.

2.3.4. Molecular dynamics simulations

All the prepared complexes, hPD-L1/BMS-202, hPD-L1/RS39, hPD-L1/P18, mPD-L1/RS39 and mPD-L1/P18, along with apo hPD-L1 (corresponding to chain A of the hPD-L1/BMS-202 crystallographic complex [19]), underwent 2 μs molecular dynamics (MD) simulations. In all cases the AMBER ff14SB [72] force field was employed for the proteins, while the latest version of the Generalized Amber Force Field [73] (GAFF2) was used for the inhibitors. RESP[74] atomic partial charges, obtained through the Antechamber accessory module of AmberTools [75], were assigned to the ligands. In detail, ab-initio Hartree-Fock [76] HF/6–31G* calculations were carried out with the revision C.01 of the Gaussian16 [77] software to compute the electrostatic potential (ESP) [78] on optimized geometries of the ligands obtained at the density functional theory (DFT) level by employing the hybrid B3LYP [79] functional. Then, RESP charges were derived through the two-stages fitting procedure implemented in Antechamber.

The leap program available in AmberTools was used to prepare each system for the MD simulations. A 12 Å layer of TIP3P [80] water molecules was added, affording a box of about ~70 Å × ~65 Å × ~85 Å. Neutrality was ensured by adding Na^+ ions, modelled with Joung and Cheatham [81,82] parameters. Finally, coordinates and topology files for the whole systems were obtained.

All the simulations were performed with Gromacs 2020.6 [83]. The Verlet cut-off scheme was used for non-bonded interactions neighbor search, the smooth Particle-Mesh Ewald [84] (SPME) method was employed for long-range electrostatic interactions, while the cut-off for long-range Van der Waals interactions was set to 1.2 nm. The equilibration protocol consisted in energy minimization followed by subsequent NVT and NPT runs. The energy minimization consisted in two steps performed by using the steepest descent algorithm: i) 20000 steps, with harmonic restraints of 1000 kJ mol^{-1} nm^{-2} applied to the ligand (when present) and to the protein heavy atoms, so that only the solvent was unconstrained; and ii) 20000 steps during which the entire system was allowed to relax. Only for these runs, a gradual decrease in the Coulomb and Lennard-Jones potentials was imposed between 1 and 1.2 nm.

For all the MD simulations (either equilibration or production), the leap-frog [85] algorithm for integrating Newton's equations of motion was used and a time step of 2 fs was chosen, while the LINCS [86] algorithm was employed to constrain bonds involving hydrogen atoms. During the MD equilibration procedure, the system was gradually heated by increasing the temperature with subsequent MD runs in the canonical ensemble (NVT) using the weak-coupling Berendsen [87] scheme. In particular, three 500 ps NVT steps were performed by gradually increasing the temperature of 100 K up to 300 K. At each step, harmonic restraints were applied to all the heavy atoms of both the protein and the inhibitor (when present), and were gradually decreased from 1000 to 500 and then to 250 kJ mol^{-1} nm^{-2}. Then, two NPT equilibration runs of 1 and 5 ns, respectively, were performed to adjust the box volume, using the Berendsen algorithm for pressure coupling. In the first NPT step, restraints of 50 kJ mol^{-1} nm^{-2} were applied on heavy atoms, while no restraints were used in the last equilibration run.

For the 2 μs production runs, temperature and pressure controls were carried-oud with the velocity-rescale [88] and Parrinello-Rhaman [89,90] scheme, respectively. All the trajectories visualization, RMSD and center of mass distances analyses were performed with the VMD [91] software. The root mean square fluctuation (RMSF) calculations and cluster analysis on the MD trajectory of the hPD-L1/BMS-202 complex were carried out using specific tools implemented in Gromacs.[83] In the latter case, the trajectory frames were clustered based on the RMSD of the binding site residues $_{A,B}$Tyr56, $_{A,B}$Glu58, $_{A,B}$Arg113, $_{A,B}$Tyr123 with a cutoff of 1.5 Å, providing two main possible protein conformations. In-house codes were used to evaluate hydrogen bonds and Pearson coefficients. The latter have been calculated according to the following equation:

$$C_{ij} = \frac{\langle (\boldsymbol{x}_i - \langle \boldsymbol{x}_i \rangle)(\boldsymbol{x}_j - \langle \boldsymbol{x}_j \rangle) \rangle}{\sigma_{\boldsymbol{x}_i} \sigma_{\boldsymbol{x}_j}},$$

where the numerator is the covariance between two variables, $\boldsymbol{x}_i$ and $\boldsymbol{x}_j$ and $\sigma_{\boldsymbol{x}_i}$ and $\sigma_{\boldsymbol{x}_j}$ are the standard deviations of each variable. The normalization obtained dividing the covariance by the product of the standard deviation of the variables allows having values ranging between -1 and +1. The variables represent the C_α atoms' positional vectors and the Pearson correlation coefficients have been evaluated between any pairs of C_α atoms. This equation has also been adapted to calculate cross-correlation coefficients among other physical quantities extracted from the MD simulations such as residues' RMSD.

All the presented figures were obtained using PyMOL [92] and the image manipulation program Gimp (2.10.22 revision 3), while the graphics were made with the Xmgrace [93] software.

3. Results and discussion

3.1. MST binding assays on human and murine PD-L1

The binding affinity (K_D) between compounds BMS-202 and RS39 and either hPD-L1 or mPD-L1 was determined by MST, a powerful technique to quantify biomolecular interactions in solution, including the affinity of low-molecular-weight binders to fluorescently labeled proteins [94]. As far as P18 is concerned, it is known to exhibit similar binding affinity to human and murine PD-L1 (K_D = 0.0883 μM and 0.174 μM, respectively) by Isothermal Calorimetry Titration (ITC) [32], and therefore it was not submitted to MST. In our assay, hPD-L1 and mPD-L1 were covalently labelled with a fluorophore to monitor the experiment. The addition of increasing concentrations of ligands altered to a different extent the thermophoretic behavior of the proteins, observed as a change of the corresponding normalized fluorescence (F_{norm}) parameter (Supplementary Fig. S2). Our data points from two independent dilution series were analyzed as previously reported [47], and the calculated K_D values are listed in Table 1. In agreement with previously reported NMR data, BMS-202 exhibited high specificity toward human versus murine PD-L1 [25]. Indeed, a K_D value of 1.1 (± 0.3) μM was determined for its interaction with hPD-L1, while no binding was observed in the case of mPD-L1. RS39 also exhibited a good degree of specificity for the human versus the murine PD-L1, with estimated K_D values of 2.8 (± 0.5) and 41 (± 9) μM, respectively. These data apparently diverge from those provided by the biochemical binding assay employed to determine the inhibitory effect of the same compounds on the hPD-1/hPD-L1 interaction (i.e. HTRF) [33]; however, they are in line with previous studies reporting K_D values of 7.2 and 8.2 μM for the hPD-1/hPD-L1 interaction measured by MST and surface plasmon resonance (SPR) techniques,

Table 1
Equilibrium dissociation constants (K_D) for the binding of BMS-202 and RS39 to hPD-L1 or mPD-L1 obtained by MST experiments.

System	K_D (μM)
BMS-202/h-PDL1	1.1 (± 0.3)
RS39/h-PDL1	2.8 (± 0.5)
BMS-202/m-PDL1	n.b.[a]
RS39/m-PDL1	41 (± 9)

[a] n.b. = no binding detected under the experimental conditions employed.

respectively [95,96]. Finally, a negative control for the interaction with both human and murine PD-L1, represented by compound **8** of our previous work [33], was also used. The measurements, carried out as described above, did not show any interaction with both the protein isoforms (Supplementary Fig. S2).

3.2. NMR spectroscopy on hPD-L1

NMR titrations were performed to confirm that the binding surface of RS39 and P18 in the hPD-L1 is mostly superimposable to that of BMS-202, identified by X-ray crystallography [19]. To this aim, the variation in signal intensity in 1D ^{1}H and 2D ^{1}H–^{15}N HSQC spectra were monitored for all three compounds. The effect observed on the 2D ^{1}H–^{15}N HSQC spectra of the protein in the presence of 12.5 μM of each ligand (protein:ligand ratio equal to 1:0.25) are shown in Fig. 2. Notably, upon addition of increasing sub-stoichiometric concentrations of each ligand, the cross-peaks of the free protein in the 2D ^{1}H–^{15}N HSQC spectrum decrease in intensity while new cross-peaks, corresponding to the protein complexed with the inhibitor, appear and increase in intensity. This indicates that the three ligands are in slow exchange on the NMR timescale.

Fig. 3 shows the per-residue intensity changes in hPD-L1 in the presence of each investigated ligand. An analysis of the amino acids exhibiting a decrease in intensity, and thus diagnostic of ligand-induced perturbation, suggests that the three compounds recognize the same region of hPD-L1 including the C, C', C'' F, G strands and the C''D loop (see Supplementary Fig. S3 for canonical Ig-strand designation). Notably, for BMS-202 the number of perturbed residues in the region comprising the C' and C'' strands and the C''D loop (a.a. 65–78) is higher than observed for the other two ligands; moreover, the cross-peaks of the free protein and of the protein bound to this ligand have similar intensities (Fig. 2a).

These data agree with the X-ray PD-L1/BMS-202 complex [19] where one molecule of ligand induces protein dimerization. Also, in the presence of P18, at the compound concentration of 12.5 μM, the signals corresponding to the free and to the bound protein are similar (Fig. 2c). As to RS39 (Fig. 2b), the signal intensity of the free protein is higher (about 75% of the total) than that of the bound protein (about 25% of the total), indicating that also RS39 binds to PD-L1, albeit with lower affinity than the other two compounds, in line with the known IC_{50} and herein measured K_D. To sum up, the three compounds bind to the same PD-L1 region (Fig. 3) and can induce to a variable extent protein dimerization upon binding, in line with previous studies [21,26,48,50].

3.3. MD simulations on hPD-L1/inhibitor complexes

The binding behavior of BMS-202, RS39 and P18 to hPD-L1 homodimer was then investigated at atomic resolution through 2 μs MD simulations. In these studies, the protein was considered in a homodimeric form based on our 2D ^{1}H–^{15}N HSQC spectra and on recent publications indicating the formation of the PD-L1 dimer in presence of small molecule ligands [21,26,48,50]. The starting MD

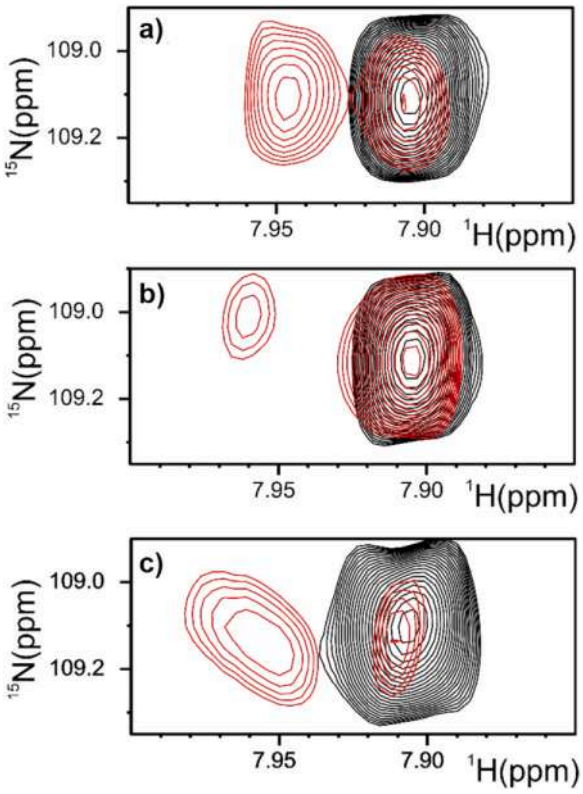

Fig. 2. Enlargement of 2D ^{1}H–^{15}N HSQC spectra of 50 μM free PD-L1 (in black) and PD-L1 upon addition of 12.5 μM BMS-202 (A), RS39 (B) and P18 (C) (in red). The displayed cross-peak is assigned to residue Gly95.

configurations, either from a crystal structure (BMS-202) or from molecular docking simulations (RS39 and P18) (see Materials and Methods), are characterized by the inhibitor accommodated at the interface between the Ig-like V-type domains of each PD-L1 monomer (referred to as chain A and B), as suggested by our 2D ^{1}H–^{15}N HSQC spectra. Here, each ligand occupies almost the same binding region, mainly surrounded by $_A$Thr20, $_{A,B}$Ile54, $_{A,B}$Tyr56, $_{A,B}$Met115, $_{A,B}$Ser117, $_{A,B}$Ala121, $_{A,B}$Asp122, $_{A,B}$Tyr123 and $_A$Lys124 (Supplementary Fig. S4), but establishing a different number of contacts depending on their size and chemical features. More in detail, the three ligands share two anchor points represented by two stacking interactions: i) a T-shaped π-π between the biphenyl moiety and $_A$Tyr56, and ii) a π-π between $_B$Tyr56 and the central aromatic ring (pyridine, triazine and chlorophenyl in BMS-202, RS39 and P18, respectively). In both BMS-202 and RS39 cases, the linear chain is involved in water-mediated interactions with $_A$Asp122 and $_A$Lys124. Notably, P18 can establish a higher number of interactions compared to the other compounds, i.e. hydrogen bonds with the $_B$Gln66 side chain and the $_A$Arg125 backbone, π-π with $_A$Tyr123 and electrostatic interactions with both $_B$Asp73 and $_A$Asp122. During MD simulations, the binding poses of the three ligands (Fig. 4) remain overall stable, in agreement with the experimentally proven capability to bind hPD-L1. However, a detailed investigation of ligands and protein behavior over time allows rationalizing the different affinity trends and understanding at molecular level the reasons behind the most perturbed 2D ^{1}H–^{15}N HSQC signals. The analysis of the RMSD of each small molecule (Fig. 5a) along its respective MD trajectory points out that the largest fluctuations are observed with RS39, in line with the lower affinity of this molecule for PD-L1 compared to BMS-202 and P18. Accordingly, the most potent compound, P18, shows the lowest RMSD values, likely due to the additional interactions that it can establish compared to the other ligands.

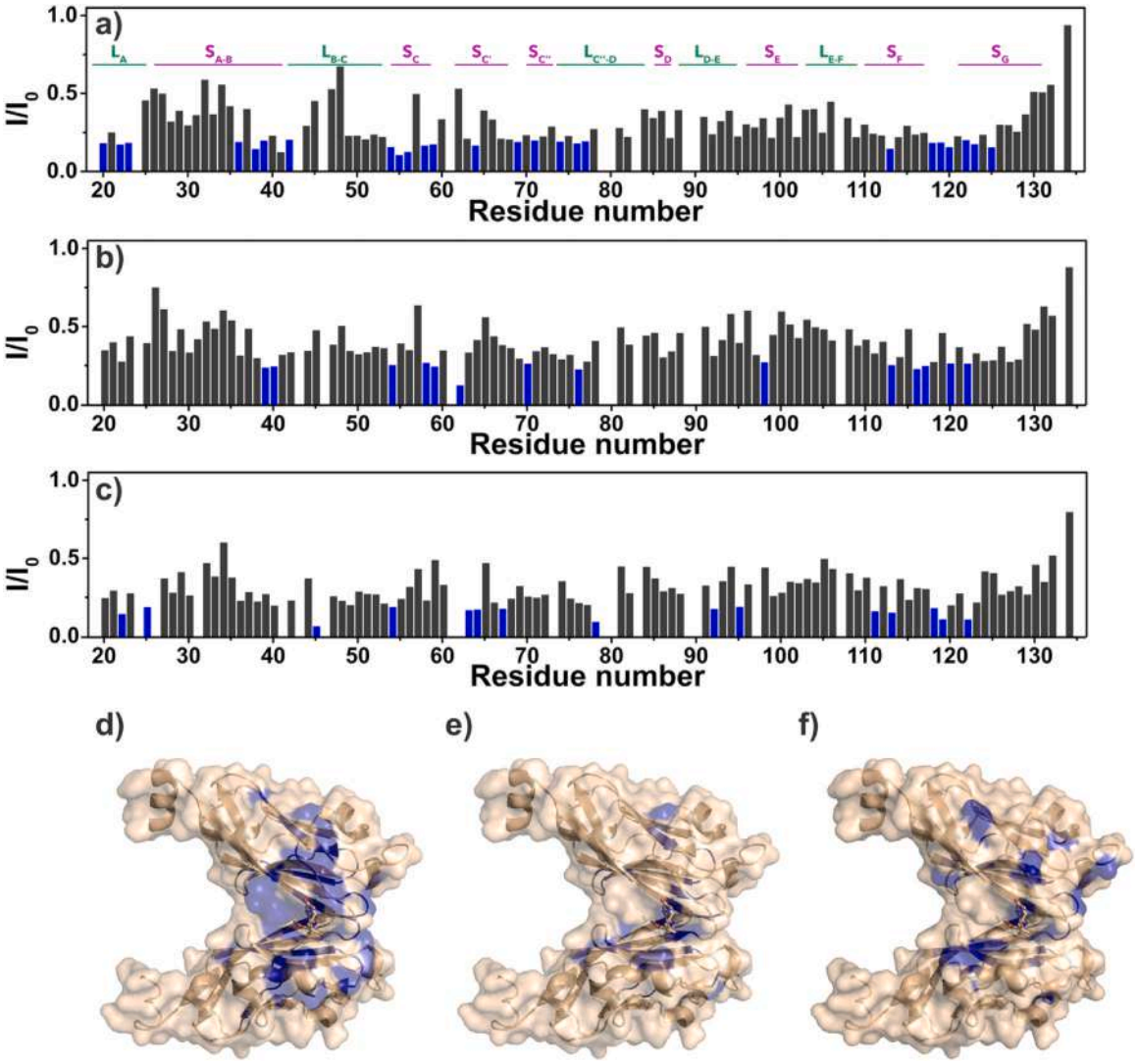

Fig. 3. Graphical representation of the per-residue intensity changes in PD-L1 in the presence of 12.5 μM BMS-202 (a, d), RS39 (b, e) and P18 (c, f). The residues exhibiting the highest decreases in signal intensities (BMS-202: Thr20, Thr22, Val23, Met36, Ile38, Glu39, Lys41, Ile54, Val55, Tyr56, Glu58, Met59, Ile64, His69, Glu71, Leu74, Val76, Gln77, Arg113, Tyr118, Gly119, Gly120, Asp122, Tyr123, Arg125; RS39: Glu39, Cys40, Ile54, Glu58, Met59, Lys64, Gly70, Val76, Ala98, Arg113, Ile116, Ser117, Gly120, Asp122; P18: Thr22, Lys25, Glu45, Ile54, Asn63, Ile64, Phe67, His78, Leu92, Gly95, Val111, Arg113, Tyr118, Gly119, Asp122) have been colored in blue in the plots (a-c) and on the X-ray structure of the protein (d-f) (PDB code: 5J89).

To better disentangle the driving forces behind these trends, we performed an RMSD analysis on each of the main functional groups of the ligands i.e. the biphenyl, the central aromatic ring and the side chain (Fig. 5b and Supplementary Fig. S5), and carefully inspected the interaction networks in which they are involved. In all cases, the RMSD values of the biphenyl group are really low, in accordance with the tight binding of this moiety to the hydrophobic pocket defined by $_{A,B}$Ile54, $_{A}$Tyr56, $_{A,B}$Met115, $_{A,B}$Ser117, $_{A,B}$Ala121 and $_{B}$Tyr123. The importance of the biphenyl moiety in small molecule PD-L1 inhibitors was already underlined in previous studies [18,19,21–23,26,31,97], and our results clearly confirm its crucial role as an anchor point for the receptor. However, our MD simulations show that, depending on the inhibitor considered, this group could interact with variable strength with the surrounding $_{A}$Tyr56, influencing in turn both its conformational freedom and interaction pattern. With BMS-202 and RS39, the T-shaped π-stacking interaction initially involving the biphenyl moiety and $_{A}$Tyr56 is weakened over time; indeed, the distance among these aromatic systems increases up to 6.5–7 Å (Supplementary Fig. S6). As a result, $_{A}$Tyr56 can rearrange and approach $_{B}$Tyr123 and $_{A}$Glu58 establishing, respectively, a π-stacking and a H-bond interaction with these residues (Supplementary Fig. S6 and S7, Table S1); in turn, $_{B}$Tyr123 is prompted to form a H-bond with $_{A}$Arg113 (Supplementary Fig. S8). Conversely, with P18, the π-stacking between the ligand's biphenyl moiety and $_{A}$Tyr56 is reinforced. As a result, $_{A}$Tyr56 cannot approach $_{B}$Tyr123 which, in turn, remains tightly bound to $_{A}$Glu58 and far from $_{A}$Arg113 (Supplementary Fig. S6–8). These differences can be probably ascribed to the larger overall volume occupied by P18, which stabilizes its interactions with the protein (in line with lowest RMSD oscillation range) and limits the conformational space explored by the surrounding $_{A}$Tyr56 and $_{B}$Tyr123 residues. In all cases, a further stabilization of the binding pose is provided by a sulfur-π interaction involving the proximal phenyl ring of the biphenyl moiety and $_{B}$Met115, retained for the 97%, 86% and 97% of the trajectories with BMS-202, RS39 and P18, respectively.

Regarding the central core of the inhibitors, it generally showed low RMSD values (< 2.5 Å), with higher oscillations observed only for the triazine ring of RS39 (Fig. 5b). Indeed, over the simulation time scale, all ligands, and in particular BMS-202 and P18, maintain a stable π-π interaction with $_{B}$Tyr56 (Supplementary Fig. S9), which has been previously reported as another important anchor point for small molecule PD-L1 binders[23,26,48]. Interestingly, the very low

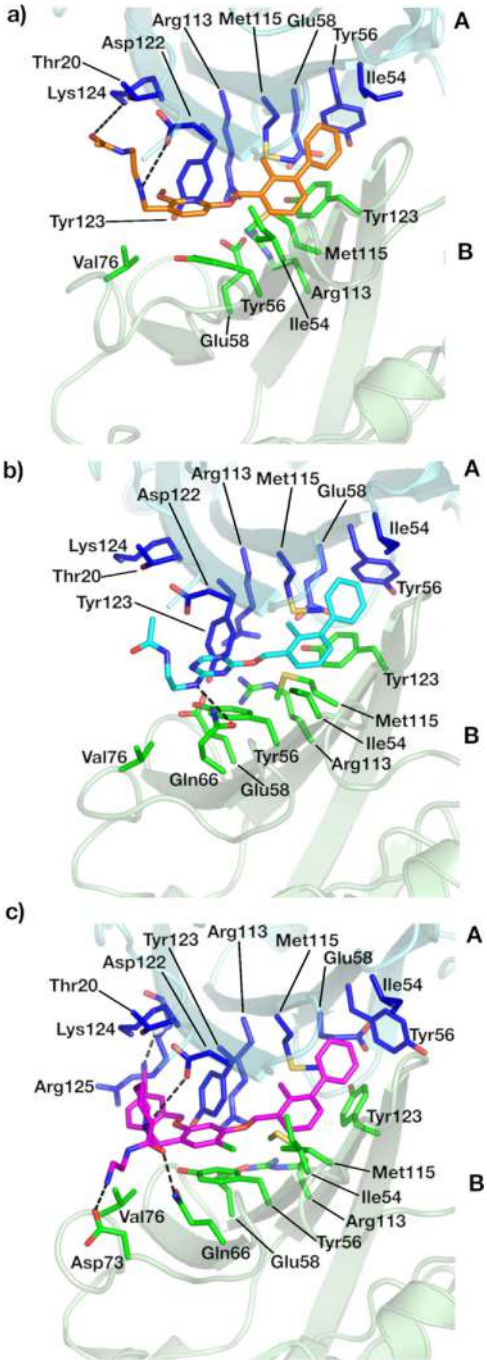

Fig. 4. Schematic representation of a) BMS-202 (orange sticks), b) RS39 (cyan sticks), and c) P18 (magenta sticks) at the binding pocket of the hPD-L1 homodimer after a 2 μs long trajectory. The main surrounding residues interacting with each ligand and participating to the homodimer stabilization are represented in blue (chain A) and green sticks (chain B). The rest of the protein is represented as a cartoon. Hydrogen atoms are hidden for clarity.

fluctuations of the P18 chlorophenyl core could be due to the establishment of additional interactions, such as the hydrogen bond between the cyanobenzyl group and the backbone of $_{B}$Arg125 and its π-π interaction with $_{A}$Tyr123 (Supplementary Fig. S10), which concertedly contribute to stabilize its binding conformation.

Finally, we evaluated the impact of the side chain on the binding dynamics of the three investigated ligands. In general, the flexibility and mobility of the linear chain, and in turn, the observed RMSD values, can be correlated with the capability of its functional groups to establish stable electrostatic or hydrophobic interactions with the surrounding residues. More in detail, the polar side chain of P18, which shows the lowest RMSD values, can form, albeit with different strength, electrostatic interactions with $_{A}$Asp122 and $_{B}$Asp73 through its piperidine and terminal amine moieties (Supplementary Fig. S11), respectively, and a hydrogen bond with $_{B}$Gln66 side chain by its amide oxygen, which is retained for about 80% of the trajectory. The side chain of BMS-202 instead forms a single electrostatic interaction with $_{A}$Asp122 (Supplementary Fig. S12) through its amine moiety and a labile hydrogen bond with the $_{A}$Lys124 side chain (detected for ~36% of the trajectory) by its amide oxygen. Finally, the RS39 side chain is not equally able to retain stable polar interactions, forming a single hydrogen bond with the $_{B}$Gln66 side chain, which is maintained in about 30% of the trajectory.

To describe the effect of the ligands on the overall protein dynamics we then measured the RMSF (Fig. 6) of each PD-L1 monomer in the different small molecule complexes over the whole MD trajectory. As expected, the largest RMSF values are found in the most flexible protein regions, i.e. the loops connecting the β-strands (18–25, 42–53, 74–85, 88–95, 103–109 residues ranges). However, it is interesting to note that also the amino acids at the 56–66 (C,C' strands) and 118–124 (F, G strands) positions show significant RMSF values. Since many of these residues ($_{A,B}$Tyr56, $_{A,B}$Glu58, $_{A,B}$Ile64, $_{A,B}$Gln66, $_{A,B}$Asp122, $_{A,B}$Tyr123, $_{A,B}$Lys124) are located in the PD-L1 binding pocket, this effect can be ascribed to the chemical perturbation induced by the investigated ligands. Nonetheless, these values are lower than in the monomeric apo hPD-L1, suggesting that both the dimerization and the ligand binding reduce the conformational freedom of these residues (see Supplementary Fig. S13). The RMSF analysis further unveils, only for BMS-202, higher fluctuations of residues ranging from 70 to 76 (chain B). This is in agreement with 2D ^{1}H–^{15}N HSQC experiments revealing that these residues are mostly perturbed in the presence of this ligand (Fig. 3). At an atomic level, the high flexibility in this protein region allows $_{B}$Ile64, $_{B}$Leu74 and $_{B}$Val76 to form a hydrophobic cage around BMS-202 (Supplementary Fig. S14), and to induce the formation of some new contacts, such as an electrostatic interaction between $_{B}$Asp73 and $_{B}$Arg82, which are instead located at ~10 Å with RS39 and P18. RMSF analysis thus suggests that ligand's affinity, and possibly the PD-L1 dimerization process, are ruled by the inhibitor capability to induce receptor conformational changes which can further stabilize the binding.

To give further insight on the protein dynamics perturbation induced by the investigated ligands, we also performed a Pearson coefficients analysis. At macroscopic level (Fig. 7), a general decrease of chain cross-correlation, especially the inter-chain, is more pronounced when moving from the less (RS39) to the more potent (P18) ligand, in line with an increasing capability to reduce the dimer dynamics. Indeed, with RS39 many positive and negative inter-chain cross correlations with Pearson coefficients larger than 0.5 (absolute values) were found among secondary structure elements (canonical Ig-strand designation is employed in the discussion).

Focusing on the binding site, the only positive correlation is found between the F strand of Chain A (comprising $_{A}$Arg113 and $_{A}$Met115) and the A loop and both the A and B strands of Chain B (encompassing residues 18–41); conversely, the C and C' strands from chain B (in particular, residues 56–66) are anti-correlated with the A and F strands from Chain A. Altogether, these data suggest a limited capability of RS39 to stabilize the hPD-L1 dimer, in line with the NMR data here reported. With BMS-202, a positive correlation occurs between the C and C'' strands from Chain A and the whole Chain B except for its C'' strand and C''-D loop (residues 72–76), to which they are instead anti-correlated. This is in line with both NMR and RMSF analyses, that highlighted these as the most flexible residues in the PD-L1/BMS-202 trimeric complex. For P18, a cross-correlated behavior is hardly detectable, except for some amino acids belonging to the binding site (residues 113–120 of F strand

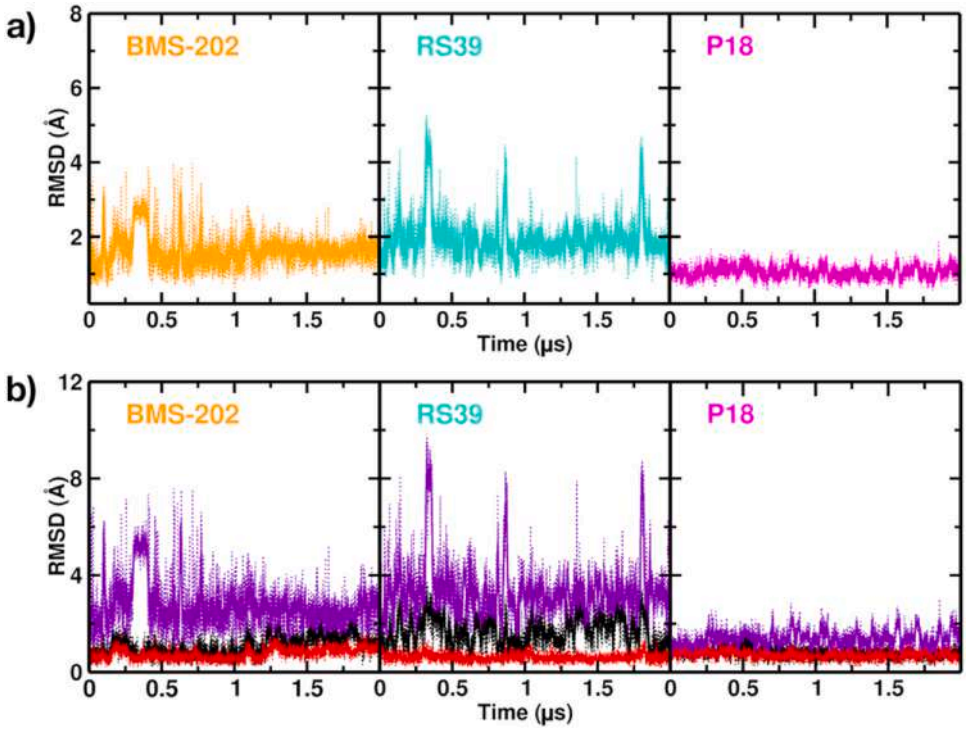

Fig. 5. a) Heavy atoms RMSD of BMS-202 (left), RS39 (center), P18 (right) shown as dots. b) RMSD of the main functional groups: biphenyl (red); BMS-202 pyridine, RS39 triazine, P18 chlorophenyl (black); linear chain, including the piperidine ring in P18, (violet). The P18 cyanobenzyl RMSD is shown in Supplementary Fig. S5. Prior to RMSD calculations, trajectories were aligned on the C_α of the secondary structural elements with respect to the initial MD frame.

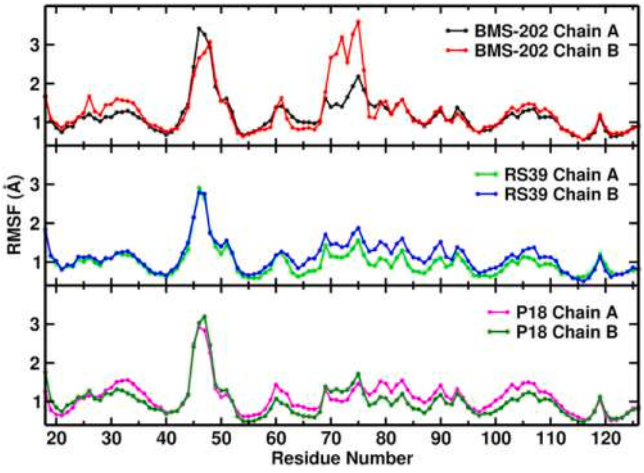

Fig. 6. hPD-L1 Chain A and Chain B residues RMSF for the three complexes (BMS-202, top; RS9, center; P18, bottom). The analysis is performed on the protein C_α atoms excluding the C-terminal residues 127–144 due to their large mobility.

from Chain A and residues 55–65 of C and C' strands from Chain B) showing positive cross-correlation. In summary, both NMR and computational outcomes suggest that the capability of each PD-L1 ligand to interact with and stabilize the receptor depends both on the number of direct contacts that it can form with the protein and the structural perturbations it can induce. An important role is played by the contacts that the small molecule inhibitor can establish with both Tyr56 and Tyr123 which can, in turn, influence the interaction network required for the hPD-L1 dimer stabilization. We also underline that tight hPD-L1 inter-chain contacts would hamper the ligand access to the binding site in a pre-existing protein dimer, in line with the hypothesis that a small molecule inhibitor would first bind to a hPD-L1 monomer and then interact with a second monomer to form a stable dimer complex [98].

3.4. MD simulations on mPD-L1/inhibitor complexes

As stated in the Introduction, despite the sequence and structural similarity (87.6%, Ig V-type domain: 19–127 amino acids), human and murine PD-L1 are characterized and diversified by few key point substitutions (see Supplementary Fig. S15 for a schematic representation). Some of these, such as Ile54Val, Asn63Gln, Arg113Cys and Met115Ile, occur at the PD-1/PD-L1 interaction surface or in its close proximity, and have been suggested, based on a static view of the protein, to impact on ligand binding and on PD-L1 dimerization [25]. However, to our knowledge, the role of these mutations in the binding event and their effect on the surrounding residues, has not been characterized in full detail. To investigate these aspects at a dynamic level, and with the aim to rationalize the different affinity profiles towards mPD-L1 of the three biphenyl ligands selected in this study, we performed 2 μs long all-atom MD simulations on the Ig V-type domain of this protein.

Due to the lack of affinity of BMS-202 for mPD-L1, we exclusively focused on RS39/ and P18/mPD-L1 trimeric complexes, which were prepared according to the procedure explained in the Materials and Methods. Notably, the initial binding pose of each ligand is highly comparable to those observed with hPD-L1. However, while the binding mode of P18 is overall retained along the whole MD trajectory, the pose of RS39 undergoes major changes, as attested by the final MD configuration (Fig. 8) and by the RMSD plots of each ligand (Fig. 9a). Indeed, the only stably anchored point of RS39 is its triazine moiety that stacks with $_B$Tyr56, although broader RMSD oscillations suggest a less tight bond compared to the human counterpart. In fact, the biphenyl moiety can move out from the hydrophobic cage defined by residues such as $_{A,B}$Val54, $_A$Tyr56, $_{A,B}$Ile115, $_{A,B}$Ser117, $_{A,B}$Ala121 and $_B$Tyr123 ($_{A,B}$Val54 and $_{A,B}$Ile115 are replaced by Ile54 and Met115 in hPD-L1, respectively) to explore a

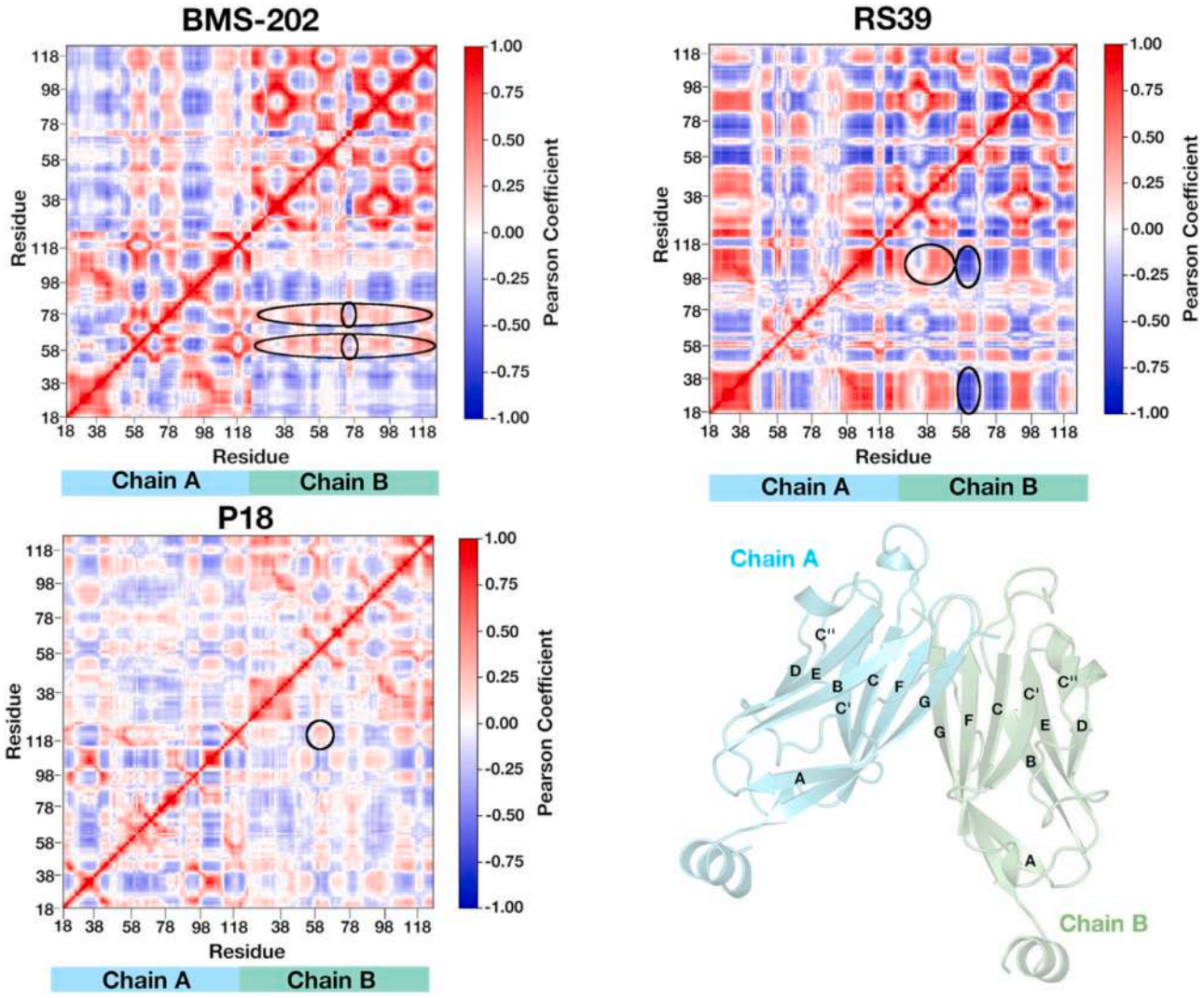

Fig. 7. Cross-correlation matrix built considering C_α atoms for the three hPD-L1 complexes. The analysis is performed on the protein C_α atoms excluding residues 127–144 due to their large mobility. Black circles indicate the inter-chain regions showing larger cross correlations in absolute value.

different cleft where it can form new interactions with residues such as $_{A,B}$Ile115, $_{A}$Tyr123 and $_{B}$Arg125 (Supplementary Fig. S16). This behavior is confirmed by the very high RMSD fluctuations of the lone biphenyl group (Fig. 9b), and is different from the hPD-L1 case, where the same moiety is highly stable in the MD timescale (Fig. 5b). It is also interesting to remark that biphenyl dynamics is found to be linearly correlated with that of the mutated residues $_{A,B}$Ile115, as testified by the positive cross-correlation coefficients of their RMSD (equal to 0.25 for $_{A}$Ile115 and 0.79 for $_{B}$Ile115, respectively); conversely, it is uncorrelated with human $_{A,B}$Met115 (RMSD correlation coefficients are in the order of 10^{-2}).

This indicates that, in mPD-L1, the displacement of the biphenyl system can depend on the different conformational landscape of Ile115 compared to Met115, as already suggested by Skalniak and coworkers through sequence alignment and docking analysis [25]. Herein, a comparison of the two molecular dynamics simulations (on human and mouse PD-L1) suggests that the Met115Ile mutation also prevents the formation of the sulfur-π interactions with the biphenyl moiety observed in the chain B of the human complex. These interactions are lost also in the P18/mPD-L1 complex, and thus contribute to explain the general loss of affinity of biphenyl ligands towards mPD-L1. Notably, our studies also suggest that biphenyl binding in mPD-L1 might also be influenced by the replacement of $_{A,B}$Arg113 with a cysteine. Indeed, this substitution implies the absence of the electrostatic contacts that are formed by $_{A,B}$Arg113 at the dimer interface in the human protein, which could, at least in part, destabilize the biphenyl binding cleft in mPD-L1.

Changes in the binding pattern of the ligands' side chain can instead be ascribed to Asn63Gln substitution. The importance of this mutation in human/murine differential ligand binding was firstly postulated by Skalniak and coworkers [25], even if its role was not deeply investigated. To this regard, our MD simulations show that with RS39 the high fluctuations of the linear chain (average RMSD ~9 Å) are correlated to that of the murine $_{B}$Gln63 (cross-correlation coefficient of 0.54), while no correlation is found with the hPD-L1 residue $_{B}$Asn63. It is interesting to note that, in addition to a direct interference with ligand binding, the $_{B}$Asn63Gln substitution contributes to altering the local arrangement of the C" strand, along with other mutations present on the C-C' β-turn, C' and C" strands and C"-D loop such as Met59Lys, Lys62Glu, Asn63Gln, Ile64Val, His69Ala, Val76Pro, Ser80Asn and Tyr81Phe. Altogether, the mutated amino acids prompt the C" strand to be more structured and the C"-D loop to be differently oriented in mPD-L1 compared to the human protein, as already noticeable in the apo state (Supplementary Fig. S18). Nonetheless, the dynamics of this protein region can be differentially modulated by the interacting ligand and vice versa. Indeed, the Asn63Gln substitution in chain B seems to increase the stability of the P18 side chain which can form an additional

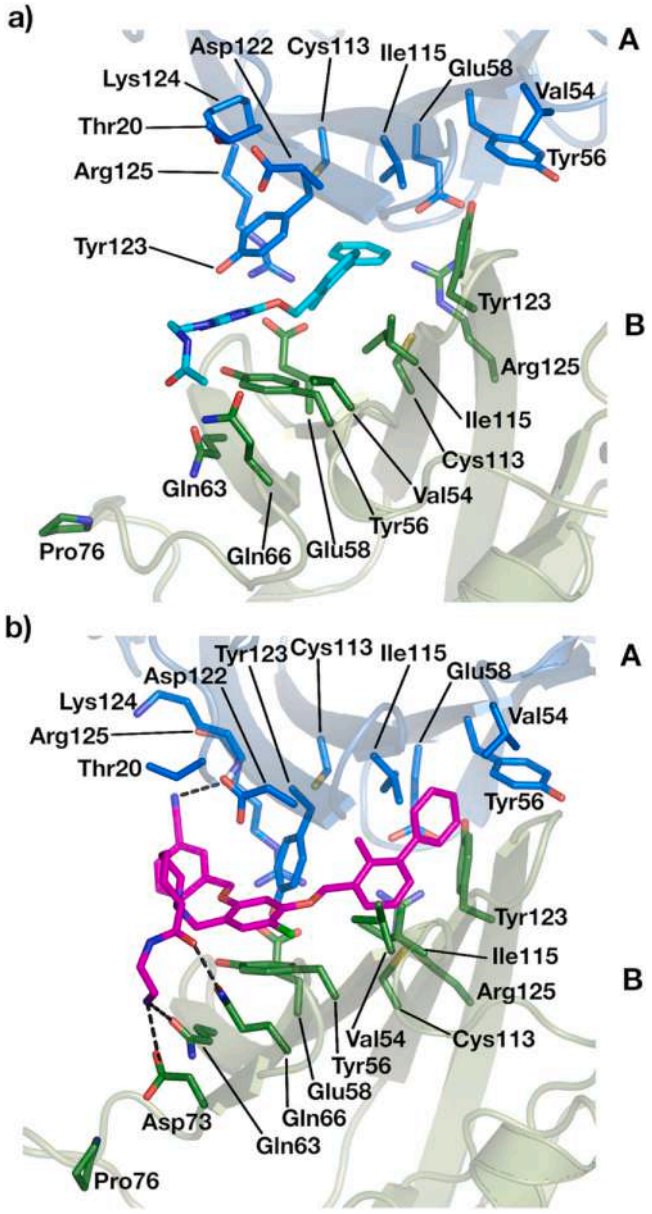

Fig. 8. Schematic representation of a) RS39 (cyan sticks), and b) P18 (magenta sticks) at the binding pocket in a mPD-L1 homodimer after a 2 μs long trajectory. The main residues interacting with each ligand and participating to homodimer stabilization are represented in blue (chain A) and green sticks (chain B). The rest of the protein is represented as a cartoon. Hydrogen atoms are hidden for clarity.

hydrogen bond with the $_{B}$Gln63 amide oxygen through its terminal amine (~38% of the trajectory). Thus, P18 seems to rigidify this subdomain through its interactions with $_{B}$Gln66 and $_{B}$Asp73, which are even reinforced with respect to the human case (80% vs. 90% and ~85% vs. ~67% of the trajectory in mPD-L1 and hPD-L1, respectively). In line with these outcomes, the RMSF analysis (Supplementary Fig. S19) of mPD-L1 highlights larger fluctuations of residues 60–80 of chain B in presence of RS39 compared to P18, reflecting its lower capability to interact with and stabilize these residues through its side chain. In summary, three single point mutations, Asn63Gln, Arg113Cys and Met115Ile, seem to be mainly responsible for the different ligand affinity towards the two species. Notably, a dynamic view of ligand binding to the two PD-L1 species reveals that the above-mentioned mutations can modulate the ligand affinity not only in a direct manner (causing steric clashes or loss of interactions, e.g. Met115Ile) but also inducing changes in the local protein

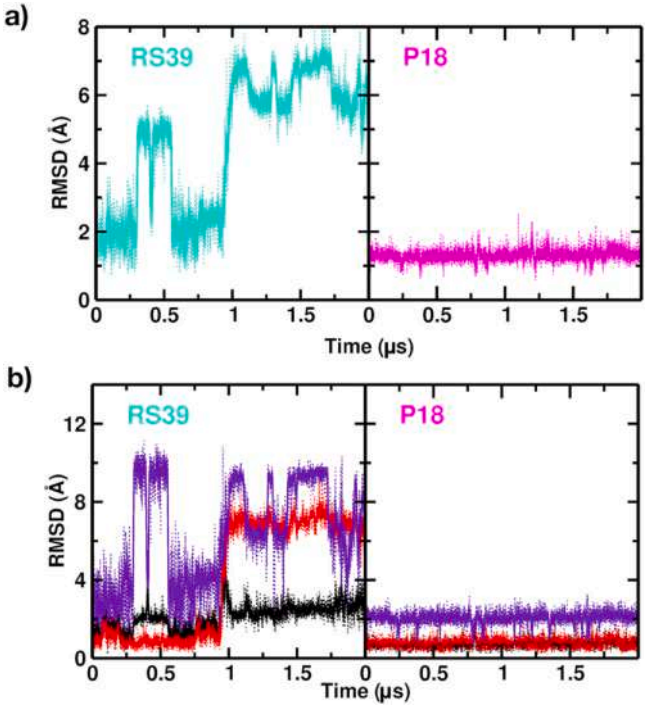

Fig. 9. a) Heavy atoms RMSD for RS39 (left) and P18 (right) shown as dots. b) RMSD of the main ligands functional groups: biphenyl (red); RS39 triazine, P18 chlorophenyl (black); linear chain, including piperidine ring in P18 case, (violet). The P18 cyanobenzyl RMSD is shown in Supplementary Fig. S17. Prior to RMSD calculations, trajectories were aligned on the C_{α} of the secondary structural elements with respect to the initial MD frame.

arrangement, in the amino acids interaction network (e.g. Asn63Gln) and even in the inter-chain dynamics at the dimer interface (e.g. Arg113Cys).

3.5. Molecular determinants for reduced/lost mPD-L1 affinity and hints for the design of novel anti-PD-L1 small molecules

The results obtained from our simulations were firstly used to rationalize, from a dynamic point of view, the complete loss of affinity of BMS-202 for mPD-L1. To this aim, we superimposed the MD final conformation of BMS-202 in complex with hPD-L1 with that of P18 in the murine protein (Fig. 10). Despite the good overlap of the two small molecules, the BMS-202 shorter polar side chain cannot reach the mouse $_{B}$Gln63, which conversely contributes to stabilize the P18 binding. More interestingly, the comparison shows that the reorientation of $_{A}$Tyr56 observed in the MD simulation of BMS-202/hPD-L1 complex would be hindered in mPD-L1 by the mutated $_{A}$Gln63, as already hypothesized by Skalniak and coworkers [25]. We remark that also the Met115Ile mutation can impact on the binding of BMS-202 to mPD-L1. Indeed, this substitution causes the loss of the peculiar sulfur-π interactions that the compound can form with both $_{A,B}$Met115, although these could be compensated by van der Waals contacts with mutated Ile.

To further extend our structure-activity relationship analysis, we also examined BMS-1166 [26], another biphenyl compound for which the inactivity towards mPD-L1 has been reported. This compound has similar size to P18, from which it differs for the presence of a 1,4-dioxane ring fused with the biphenyl group and for the nature of the polar side chain. A superposition between the hPD-L1/BMS-1166 X-ray complex (PDB code: 6R3K [26]) and the MD conformation of the P18/mPD-L1 trimer (see Fig. 10) shows that, in the murine protein, the 1,4-dioxane would clash with $_{A}$Tyr56, whose conformational freedom is limited in mouse by the mutated Gln63. As seen for BMS-202, the

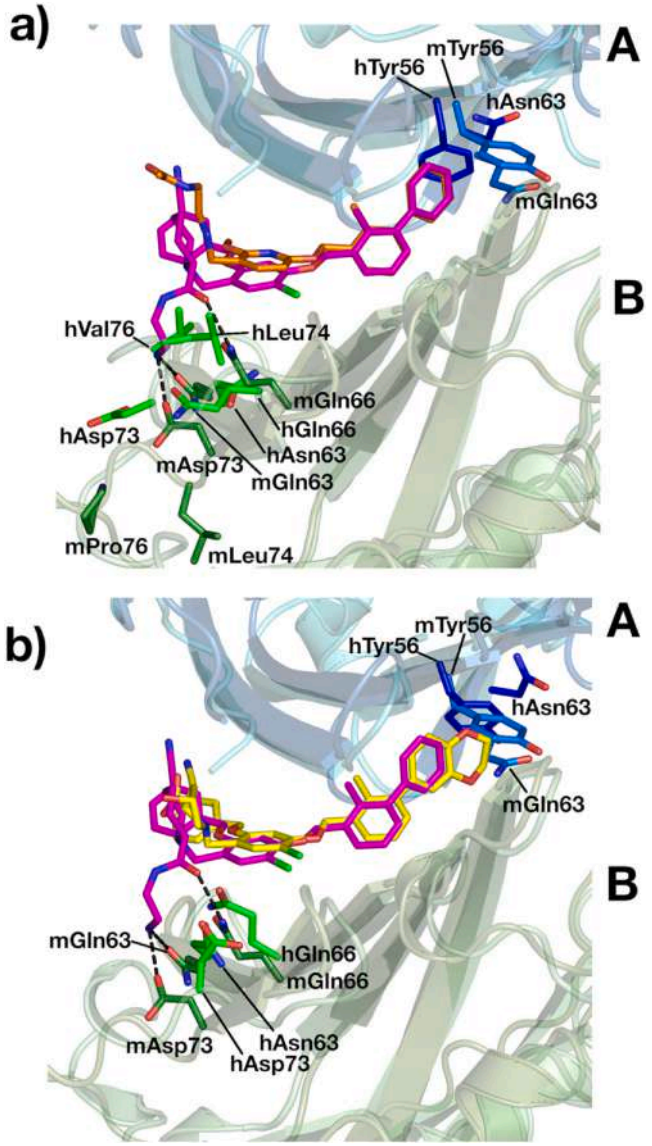

Fig. 10. Superposition of the last frame of the P18/mPD-L1 MD simulation with: a) BMS-202/hPD-L1 (final MD conformation); b) BMS-1166/hPD-L1 (crystal structure, PDB code: 6R3K). P18, BMS-202 and BMS-1166 are shown in magenta, orange and yellow sticks, respectively. The residues mainly contributing to binding affinity differences between the two species are shown as blue and marine blue sticks for chain A of hPD-L1 and mPD-L1, respectively, and green and forest green sticks for chain B of hPD-L1 and mPD-L1, respectively. The tertiary structure of both the proteins is represented as a cartoon. Hydrogen atoms are hidden for clarity.

shorter length and the different electrostatic nature of the side chain would not allow BMS-1166 to establish the same stabilizing interactions formed by P18 (see Fig. 10). This analysis supports our MD results showing that, while in mPD-L1 the $_{A}$Tyr56 flexibility is highly limited, in hPD-L1 the same residue seems to be intrinsically flexible and able to adapt to the incoming ligand. Indeed, in the presence of P18, which is tightly anchored to the binding surface, $_{A}$Tyr56 is highly stable in its position stacking with terminal phenyl of the ligand (superimposable to that of the BMS-202 X-ray complex). Conversely, in the MD simulation of RS39, showing higher fluctuations than P18 at the binding surface, the $_{A}$Tyr56 bends against the $_{A}$Asn63 opening up an amphipathic tunnel (Supplementary Fig. S6 and S20). The existence of this channel, which is nearly symmetrical to the area hosting the polar chain of BMS-202, has been previously disclosed by X-ray structures of both BMS-1166 and C2-symmetric inhibitors such as LH1307 (PDB codes: 6R3K and 6RPG [22], respectively). In spite of these observations, to date, most of the available anti-hPD-L1 agents are "short" molecules (see Fig. 1, "first generation") that cannot target this additional protein region. On the other hand, compounds "extended" either symmetrically or asymmetrically (i.e. featuring either the same or different branches on the two sides, respectively) are now emerging as "second generation" anti-hPD-L1 ligands, however they are still a minority. To investigate in more detail here the differences between the "short" and the "extended" molecules in the interaction with PD-L1, four representative compounds, featuring two (INCB086550 [38] and GS-4224 [39]), three (BMS-1058) [54] or four branches (BMS-40770) [53] were docked (Fig. 11 and Supplementary Fig. S21) in the crystal structure of hPD-L1 in complex with LH1307 (PDB code: 6RPG).

Docking results allowed us to generate a 5-points pharmacophore model fitting into the five sites of the bone-shaped PD-L1 dimer pocket. The main anchor point is represented by the biphenyl-containing system; herein, the presence of two aromatic rings next to the biphenyl core allows engaging, at the same time, Tyr56 from both monomer A and B. The other four points are represented by the two polar side chains, which can contact Thr20, Asp122, and Lys124 of each monomer and, when present, by the additional cyanopyridine ring (or by any other aromatic ring substituted with a H-bond acceptor) that can simultaneously interact with Tyr123 from both monomers (Supplementary Fig. S21). Remarkably, our MD simulations show that this would not happen with smaller ligands such as BMS-202, which can only interact with $_{B}$Tyr56. Along the same line, the absence of a second polar side chain does not allow "short" ligands to form the aforementioned electrostatic contacts (with Thr20, Asp122, Lys124) in both PD-L1 monomers. A more dynamic view of the 5-points pharmacophore model was obtained through an ensemble docking approach, using frames extracted from the MD trajectory of the hPD-L1/BMS-202 (see Materials and Methods for details). In particular, docking of "extended" ligands INCB086550 and GS-4224 in the most representative protein conformation provided poses superimposable to those obtained using the X-ray structure (see Supplementary Fig. S22). Interestingly, both these PD-L1 structures show $_{A}$Tyr56 in the same orientation, which allows the opening of the amphiphilic channel and, in turn, the accommodation of "extended" ligands.

Thanks to the additional interactions established with hPD-L1, "extended" ligands could in principle display not only an improved potency but also a prolonged residence time, so as to stabilize more efficiently the PD-L1 dimer, which is required to inhibit the interaction with PD-1 in vivo. In fact, although in HTRF assays the IC_{50}s of "short" and "extended" ligands are in some cases comparable [99], the latter ones perform much better in cell-based assays.[22] Also, in light of their larger volume and the more demanding steric and electrostatic requirements, "extended" compounds can offer higher specificity towards the PD-L1 compared to "short" molecules that may more easily bind to the binding pocket of other receptors; this might, in turn, lead to reduced off-target, or more generally toxic, effects. Altogether, these considerations would possibly explain why the "extended" INCB086550 is the most advanced compound in the complex clinical trial pathway (successfully accomplished Phase I clinical studies). Finally, although the dual activity on hPD-L1 and mPD-L1 is surely desirable to speed up preclinical research for putative inhibitors, this aim is challenged by the mutations occurring at the binding site of the murine protein. Indeed, such substitutions can especially affect the flexibility of Tyr56 with respect to hPD-L1, so that, in mPD-L1, the access to above-mentioned channel would be precluded to "extended" ligands. On the other hand, doubly branched "short" ligands like P18, which are endowed with both an aromatic and a highly polar chain, can overcome the detrimental effect of the mutations by tightly interacting with mPD-L1. Altogether, molecular dynamics and docking studies, supported by MST assays and NMR experiments, have here unraveled the structural

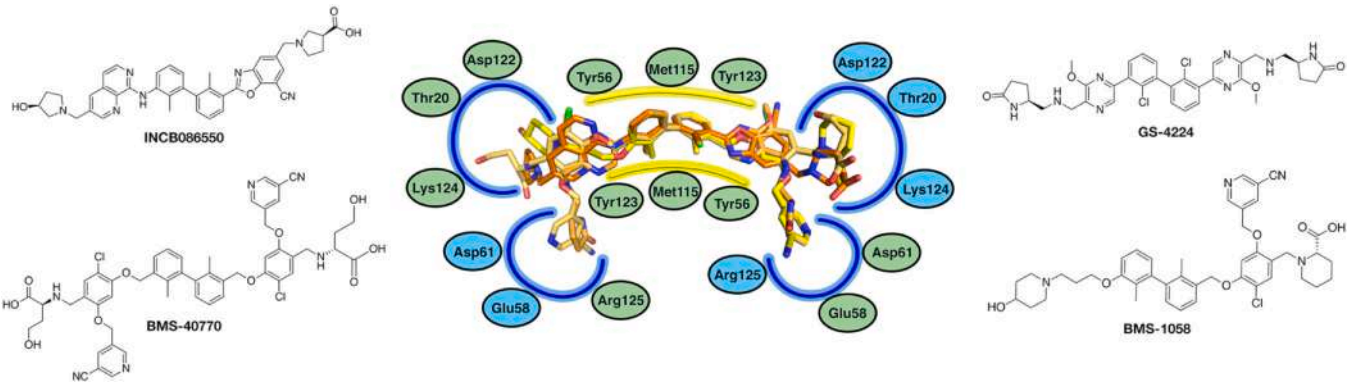

Fig. 11. Schematic sticks representation of INCB086550 (orange), GS-4224 (bright orange), BMS-40770 (yellow orange) and BMS-1058 (yellow) conformations obtained from molecular docking simulations in the hPD-L1 crystal structure (PDB Code: 6RPG) as a 5-points pharmacophore model fitted in the "bone-shaped" receptor pocket, along with the main residues involved in specific interactions with the ligands (light blue ellipses for residues belonging to the A chain and green ellipses for residues belonging to the B chain). The chemical structures of the investigated ligands are also shown.

determinants of the species' specificity of PD-L1 ligands, providing clues that may assist medicinal chemists to design the next generation of small molecule drugs.

4. Conclusions

In this study, using a combined experimental and computational approach, we have provided a molecular description of the binding behavior of the biphenyl-based compounds BMS-202, RS39 and P18 to human and murine PD-L1, also unveiling the main determinants for their different affinity profile towards the human protein and for their reduced potency towards the mouse orthologue. In particular, we have shown that the specific size and nature of the inhibitor can influence not only the number of interactions that it can establish at the PD-L1 dimer interface, but also the protein inter-chain dynamics and stabilization. A crucial role in these events is also played by single point mutations, which diversify the two proteins, occurring both in proximity and far from the ligand binding site. The extensive analysis of hPD-L1 MD simulations performed with "short" ligands and the docking studies on the "extended" compounds provided results that can be used to guide the design of future PD-L1 inhibitors.

Funding Sources

This research was funded by the Italian Ministry of Education, University, and Research (MIUR), Progetti di Rilevante Interesse Nazionale (PRIN) 2017 (2017PHRC8X). We also acknowledge Regione Campania–POR Campania FESR 2014/2020 (B61G18000470007) and "Progetto Dipartimenti di Eccellenza 2023–2027 (DICUS2.0)".

Supplementary data

Supplementary data to this article can be found online at XXX:

MicroScale Thermophoresis binding assay curves, supplementary plots, tables and figures about the MD simulations, additional docking calculations on "extended ligands" (PDF).

PDB coordinates of the presented computational models (PDB).

CRediT authorship contribution statement

G.D. and V.M.D.A: investigation, formal analysis, writing – original draft; P.R.: investigation, formal analysis; L.C. and J.A.: validation, supervision, writing – original draft; S.M., M.S., D.R. and G.A.: investigation; M.F.: supervision, writing – review & editing; A.C., V.L.P, D.A. and P.S.: writing – review & editing; D.B.: supervision, writing – review & editing; F.S.D.L: conceptualization, supervision, writing – review & editing; L.M.: project administration, funding acquisition.

Declaration of Competing Interest

The authors declare that they have no known competing financial interests or personal relationships that could have appeared to influence the work reported in this paper.

Acknowledgements

The authors acknowledge the support and the use of resources of Instruct-ERIC, a landmark ESFRI project, and specifically the CERM/CIRMMP Italy centre.

Author Contributions

The manuscript was written through contributions of all authors. All authors have given approval to the final version of the manuscript.

Appendix A. Supporting information

Supplementary data associated with this article can be found in the online version at doi:10.1016/j.csbj.2023.06.006.

References

[1] Ganesan A, Ahmed M, Okoye I, Arutyunova E, Babu D, Turnbull WL, et al. Comprehensive in vitro characterization of PD-L1 small molecule inhibitors. Sci Rep 2019;9:12392. https://doi.org/10.1038/s41598-019-48826-6
[2] Surmiak E, Magiera-Mularz K, Musielak B, Muszak D, Kocik-Krol J, Kitel R, et al. PD-L1 inhibitors: different classes, activities, and mechanisms of action. Int J Mol Sci 2021;22:11797. https://doi.org/10.3390/ijms222111797
[3] Romagnani S. Immunological tolerance and autoimmunity. Intern Emerg Med 2006;1:187–96. https://doi.org/10.1007/BF02934736
[4] Walker LSK, Abbas AK. The enemy within: keeping self-reactive T cells at bay in the periphery. Nat Rev Immunol 2002;2:11–9. https://doi.org/10.1038/nri701
[5] Topalian SL, Drake CG, Pardoll DM. Immune checkpoint blockade: a common denominator approach to cancer therapy. Cancer Cell 2015;27:450–61. https://doi.org/10.1016/j.ccell.2015.03.001
[6] Zitvogel L, Tesniere A, Kroemer G. Cancer despite immunosurveillance: immunoselection and immunosubversion. Nat Rev Immunol 2006;6:715–27. https://doi.org/10.1038/nri1936
[7] Azuma T, Yao S, Zhu G, Flies AS, Flies SJ, Chen L. B7-H1 is a ubiquitous antiapoptotic receptor on cancer cells. Blood 2008;111:3635–43. https://doi.org/10.1182/blood-2007-11-123141
[8] Francisco LM, Salinas VH, Brown KE, Vanguri VK, Freeman GJ, Kuchroo VK, et al. PD-L1 regulates the development, maintenance, and function of induced regulatory T cells. J Exp Med 2009;206:3015–29. https://doi.org/10.1084/jem.20090847

[9] Han Y, Liu D, Li L. PD-1/PD-L1 pathway: current researches in cancer. Am J Cancer Res 2020;10:727–42.
[10] Ricklefs FL, Alayo Q, Krenzlin H, Mahmoud AB, Speranza MC, Nakashima H, et al. Immune evasion mediated by PD-L1 on glioblastoma-derived extracellular vesicles. Sci Adv 2018:4. https://doi.org/10.1126/sciadv.aar2766
[11] Sun S, Fei X, Mao Y, Wang X, Garfield DH, Huang O, et al. PD-1+ immune cell infiltration inversely correlates with survival of operable breast cancer patients. Cancer Immunol, Immunother 2014;63:395–406. https://doi.org/10.1007/s00262-014-1519-x
[12] Sun L, Zhang L, Yu J, Zhang Y, Pang X, Ma C, et al. Clinical efficacy and safety of anti-PD-1/PD-L1 inhibitors for the treatment of advanced or metastatic cancer: a systematic review and meta-analysis. Sci Rep 2020;10:2083. https://doi.org/10.1038/s41598-020-58674-4
[13] Patnaik A, Kang SP, Rasco D, Papadopoulos KP, Elassaiss-Schaap J, Beeram M, et al. Phase I study of pembrolizumab (MK-3475; Anti-PD-1 monoclonal antibody) in patients with advanced solid tumors. Clin Cancer Res 2015;21:4286–93. https://doi.org/10.1158/1078-0432.CCR-14-2607
[14] Topalian SL, Hodi FS, Brahmer JR, Gettinger SN, Smith DC, McDermott DF, et al. Safety, activity, and immune correlates of anti–PD-1 antibody in cancer. N Engl J Med 2012;366:2443–54. https://doi.org/10.1056/NEJMoa1200690
[15] Brahmer JR, Tykodi SS, Chow LQM, Hwu W-J, Topalian SL, Hwu P, et al. Safety and activity of anti–PD-L1 antibody in patients with advanced cancer. N Engl J Med 2012;366:2455–65. https://doi.org/10.1056/NEJMoa1200694
[16] Constantinidou A, Alifieris C, Trafalis DT. Targeting programmed cell death -1 (PD-1) and ligand (PD-L1): a new era in cancer active immunotherapy. Pharm Ther 2019;194:84–106. https://doi.org/10.1016/j.pharmthera.2018.09.008
[17] Rizzo D, Cerofolini L, Giuntini S, Iozzino L, Pergola C, Sacco F, et al. Epitope mapping and binding assessment by solid-state NMR provide a way for the development of biologics under the quality by design paradigm. J Am Chem Soc 2022;144:10006–16. https://doi.org/10.1021/jacs.2c03232
[18] L.S. Chupak X. Zheng Compounds useful as immunomodulators. WO2015034820A1, 2015.
[19] Zak KM, Grudnik P, Guzik K, Zieba BJ, Musielak B, Dömling A, et al. Structural basis for small molecule targeting of the programmed death ligand 1 (PD-L1). Oncotarget 2016;7:30323–35. https://doi.org/10.18632/oncotarget.8730
[20] Skalniak L, Zak KM, Guzik K, Magiera K, Musielak B, Pachota M, et al. Small-molecule inhibitors of PD-1/PD-L1 immune checkpoint alleviate the PD-L1-induced exhaustion of T-cells. Oncotarget 2017;8:72167–81. https://doi.org/10.18632/oncotarget.20050
[21] Guzik K, Zak KM, Grudnik P, Magiera K, Musielak B, Törner R, et al. Small-molecule inhibitors of the programmed cell death-1/programmed death-ligand 1 (PD-1/PD-L1) interaction via transiently induced protein states and dimerization of PD-L1. J Med Chem 2017;60:5857–67. https://doi.org/10.1021/acs.jmedchem.7b00293
[22] Basu S, Yang J, Xu B, Magiera-Mularz K, Skalniak L, Musielak B, et al. Design, synthesis, evaluation, and structural studies of C2-symmetric small molecule inhibitors of programmed cell death-1/programmed death-ligand 1 protein––protein interaction. J Med Chem 2019;62:7250–63. https://doi.org/10.1021/acs.jmedchem.9b00795
[23] Konieczny M, Musielak B, Kocik J, Skalniak L, Sala D, Czub M, et al. Di-bromo-based small-molecule inhibitors of the PD-1/PD-L1 immune checkpoint. J Med Chem 2020;63:11271–85. https://doi.org/10.1021/acs.jmedchem.0c01260
[24] Hu Z, Yu P, Du G, Wang W, Zhu H, Li N, et al. PCC0208025 (BMS202), a small molecule inhibitor of PD-L1, produces an antitumor effect in B16-F10 melanoma-bearing mice. PLoS One 2020;15:e0228339.
[25] Magiera-Mularz K, Kocik J, Musielak B, Plewka J, Sala D, Machula M, et al. Human and mouse PD-L1: similar molecular structure, but different druggability profiles. IScience 2021;24:101960. https://doi.org/10.1016/j.isci.2020.101960
[26] Muszak D, Surmiak E, Plewka J, Magiera-Mularz K, Kocik-Krol J, Musielak B, et al. Terphenyl-based small-molecule inhibitors of programmed cell death-1/programmed death-ligand 1 protein–protein interaction. J Med Chem 2021;64:11614–36. https://doi.org/10.1021/acs.jmedchem.1c00957
[27] Chai I, Kornyeyev D, Hsieh E, Magombedze G, Stapleton L, Hung M, et al. Effects of small molecule-induced dimerization on the programmed death ligand 1 protein life cycle. Sci Rep 2022;12:21286. https://doi.org/10.1038/s41598-022-25417-6
[28] Sun C, Yin M, Cheng Y, Kuang Z, Liu X, Wang G, et al. Novel small-molecule PD-L1 inhibitor induces PD-L1 internalization and optimizes the immune microenvironment. J Med Chem 2023;66:2064–83. https://doi.org/10.1021/acs.jmedchem.2c01801
[29] P.G.N. Sasikumar M. Ramachandra S.S.S. Naremaddepalli 1,2,4-oxadiazole derivatives as immunomodulators. WO2015033299A1, 2015.
[30] Zhan M-M, Hu X-Q, Liu X-X, Ruan B-F, Xu J, Liao C. From monoclonal antibodies to small molecules: the development of inhibitors targeting the PD-1/PD-L1 pathway. Drug Discov Today 2016;21:1027–36. https://doi.org/10.1016/j.drudis.2016.04.011
[31] Guzik K, Tomala M, Muszak D, Konieczny M, Hec A, Błaszkiewicz U, et al. Development of the inhibitors that target the PD-1/PD-L1 interaction—a brief look at progress on small molecules, peptides and macrocycles. Molecules 2019;24:2071. https://doi.org/10.3390/molecules24112071
[32] Cheng B, Wang W, Niu X, Ren Y, Liu T, Cao H, et al. Discovery of novel and highly potent resorcinol dibenzyl ether-based PD-1/PD-L1 inhibitors with improved drug-like and pharmacokinetic properties for cancer treatment. J Med Chem 2020;63:15946–59. https://doi.org/10.1021/acs.jmedchem.0c01684
[33] Russomanno P, Assoni G, Amato J, D'Amore VM, Scaglia R, Brancaccio D, et al. Interfering with the tumor–immune interface: making way for triazine-based small molecules as novel PD-L1 inhibitors. J Med Chem 2021;64:16020–45. https://doi.org/10.1021/acs.jmedchem.1c01409
[34] Butera R, Ważyńska M, Magiera-Mularz K, Plewka J, Musielak B, Surmiak E, et al. Design, synthesis, and biological evaluation of imidazopyridines as PD-1/PD-L1 antagonists. ACS Med Chem Lett 2021;12:768–73. https://doi.org/10.1021/acsmedchemlett.1c00033
[35] Wang T, Cai S, Cheng Y, Zhang W, Wang M, Sun H, et al. Discovery of small-molecule inhibitors of the PD-1/PD-L1 axis that promote PD-L1 internalization and degradation. J Med Chem 2022;65:3879–93. https://doi.org/10.1021/acs.jmedchem.1c01682
[36] Wang Y, Kun Huang Gao Y, Yuan D, Ling L, Liu J, et al. Discovery of quinazoline derivatives as novel small-molecule inhibitors targeting the programmed cell death-1/programmed cell death-ligand 1 (PD-1/PD-L1) interaction. Eur J Med Chem 2022;229:113998. https://doi.org/10.1016/j.ejmech.2021.113998
[37] Zwergel C, Fioravanti R, Mai A. PD-L1 small-molecule modulators: a new hope in epigenetic-based multidrug cancer therapy? Drug Discov Today 2023;28:103435. https://doi.org/10.1016/j.drudis.2022.103435
[38] L. Wu J. Li C. Qi et al. Benzooxazole derivatives as immunomodulators. WO2018119266, 2018.
[39] E. Aktoudianakis T. Appleby A. Cho et al.PD-1/PD-L1 inhibitors. WO2018195321, 2018 .
[40] Clinicaltrials.govStudy of INCB086550 in select solid tumors, 2020.
[41] Offringa R, Kötzner L, Huck B, Urbahns K. The expanding role for small molecules in immuno-oncology. Nat Rev Drug Discov 2022;21:821–40. https://doi.org/10.1038/s41573-022-00538-9
[42] Wang T, Cai S, Wang M, Zhang W, Zhang K, Chen D, et al. Novel biphenyl pyridines as potent small-molecule inhibitors targeting the programmed cell death-1/programmed cell death-ligand 1 interaction. J Med Chem 2021;64:7390–403. https://doi.org/10.1021/acs.jmedchem.1c00010
[43] Acúrcio RC, Pozzi S, Carreira B, Pojo M, Gómez-Cebrián N, Casimiro S, et al. Therapeutic targeting of PD-1/PD-L1 blockade by novel small-molecule inhibitors recruits cytotoxic T cells into solid tumor microenvironment. J Immunother Cancer 2022;10:e004695. https://doi.org/10.1136/jitc-2022-004695
[44] de La Rochere P, Guil-Luna S, Decaudin D, Azar G, Sidhu SS, Piaggio E. Humanized mice for the study of immuno-oncology. Trends Immunol 2018;39:748–63. https://doi.org/10.1016/j.it.2018.07.001
[45] Zitvogel L, Pitt JM, Daillère R, Smyth MJ, Kroemer G. Mouse models in oncoimmunology. Nat Rev Cancer 2016;16:759–73. https://doi.org/10.1038/nrc.2016.91
[46] Sun C, Cheng Y, Liu X, Wang G, Min W, Wang X, et al. Novel phthalimides regulating PD-1/PD-L1 interaction as potential immunotherapy agents. Acta Pharm Sin B 2022;12:4446–57. https://doi.org/10.1016/j.apsb.2022.04.007
[47] Amato J, Madanayake TW, Iaccarino N, Novellino E, Randazzo A, Hurley LH, et al. HMGB1 binds to the *KRAS* promoter G-quadruplex: a new player in oncogene transcriptional regulation? Chem Commun 2018;54:9442–5. https://doi.org/10.1039/C8CC03614D
[48] Bailly C, Vergoten G. Protein homodimer sequestration with small molecules: Focus on PD-L1. Biochem Pharm 2020;174:113821. https://doi.org/10.1016/j.bcp.2020.113821
[49] Guo Y, Jin Y, Wang B, Liu B. Molecular mechanism of small-molecule inhibitors in blocking the PD-1/PD-L1 pathway through PD-L1 dimerization. Int J Mol Sci 2021;22:4766. https://doi.org/10.3390/ijms22094766
[50] Park J-J, Thi EP, Carpio VH, Bi Y, Cole AG, Dorsey BD, et al. Checkpoint inhibition through small molecule-induced internalization of programmed death-ligand 1. Nat Commun 2021;12:1222. https://doi.org/10.1038/s41467-021-21410-1
[51] M.M. Miller et al. Preparation of macrocyclic peptides as inhibitors of the PD-1/PD-L1 and CD80(B7-1)/PD-L1 protein/protein interactions for treating cancers and infections. US20140294898A1, 2014.
[52] M.M. Miller et al. Macrocyclic inhibitors of the PD1/PDL1 and CD80 (B7-1)/PD-L1 protein/protein interactions. WO2016039749A1, 2016.
[53] K. Yeung K.A. Grant-Young J. Zhu et al. Biaryl compounds useful as immunomodulators. WO2018044963A1, 2018.
[54] Yeung K., Connolly T. P., Frennesson D. B. et al. Compounds useful as immunomodulators. WO2017066227A1, 2017.
[55] Maestro, Schrödinger, LLC, New York, NY, 2021.
[56] Protein Preparation Wizard, Schrödinger, LLC, New York, NY, 2021.
[57] Prime, Schrödinger, LLC, New York, NY, 2021.
[58] Jacobson MP, Pincus DL, Rapp CS, Day TJF, Honig B, Shaw DE, et al. A hierarchical approach to all-atom protein loop prediction. Protein: Struct, Funct, Bioinforma 2004;55:351–67. https://doi.org/10.1002/prot.10613
[59] Jacobson MP, Friesner RA, Xiang Z, Honig B. On the role of the crystal environment in determining protein side-chain conformations. J Mol Biol 2002;320:597–608. https://doi.org/10.1016/S0022-2836(02)00470-9
[60] Olsson MHM, Søndergaard CR, Rostkowski M, Jensen JH. PROPKA3: consistent treatment of internal and surface residues in empirical p K_a predictions. J Chem Theory Comput 2011;7:525–37. https://doi.org/10.1021/ct100578z
[61] Banks JL, Beard HS, Cao Y, Cho AE, Damm W, Farid R, et al. Integrated modeling program, applied chemical theory (IMPACT). J Comput Chem 2005;26:1752–80. https://doi.org/10.1002/jcc.20292
[62] LigPrep, Schrödinger, LLC, New York, NY, 2021.
[63] Greenwood JR, Calkins D, Sullivan AP, Shelley JC. Towards the comprehensive, rapid, and accurate prediction of the favorable tautomeric states of drug-like molecules in aqueous solution. J Comput Aided Mol Des 2010;24:591–604. https://doi.org/10.1007/s10822-010-9349-1
[64] Shelley JC, Cholleti A, Frye LL, Greenwood JR, Timlin MR, Uchimaya M. Epik: a software program for pK a prediction and protonation state generation for drug-

like molecules. J Comput Aided Mol Des 2007;21:681–91. https://doi.org/10.1007/s10822-007-9133-z
[65] Epik, Schrödinger, LLC, New York, NY, 2021.
[66] MacroModel, Schrödinger, LLC, New York, NY, 2021.
[67] Friesner RA, Murphy RB, Repasky MP, Frye LL, Greenwood JR, Halgren TA, et al. Extra precision glide: docking and scoring incorporating a model of hydrophobic enclosure for protein–ligand complexes. J Med Chem 2006;49:6177–96. https://doi.org/10.1021/jm051256o
[68] Halgren TA, Murphy RB, Friesner RA, Beard HS, Frye LL, Pollard WT, et al. Glide: a new approach for rapid, accurate docking and scoring. 2. enrichment factors in database screening. J Med Chem 2004;47:1750–9. https://doi.org/10.1021/jm030644s
[69] Friesner RA, Banks JL, Murphy RB, Halgren TA, Klicic JJ, Mainz DT, et al. Glide: a new approach for rapid, accurate docking and scoring. 1. method and assessment of docking accuracy. J Med Chem 2004;47:1739–49. https://doi.org/10.1021/jm0306430
[70] Glide, Schrödinger, LLC, New York, NY, 2021.
[71] Lim H, Chun J, Jin X, Kim J, Yoon J, No KT. Investigation of protein-protein interactions and hot spot region between PD-1 and PD-L1 by fragment molecular orbital method. Sci Rep 2019;9:16727. https://doi.org/10.1038/s41598-019-53216-z
[72] Maier JA, Martinez C, Kasavajhala K, Wickstrom L, Hauser KE, Simmerling C. ff14SB: Improving the Accuracy of Protein Side Chain and Backbone Parameters from ff99SB. J Chem Theory Comput 2015;11:3696–713. https://doi.org/10.1021/acs.jctc.5b00255
[73] Wang J, Wolf RM, Caldwell JW, Kollman PA, Case DA. Development and testing of a general amber force field. J Comput Chem 2004;25:1157–74. https://doi.org/10.1002/jcc.20035
[74] Bayly CI, Cieplak P, Cornell W, Kollman PA. A well-behaved electrostatic potential based method using charge restraints for deriving atomic charges: the RESP model. J Phys Chem 1993;97:10269–80. https://doi.org/10.1021/j100142a004
[75] Case DA, Ben-Shalom IY, Brozell SR, et al. AMBER 2018. San Francisco: University of California; 2018.
[76] Roothaan CCJ. New developments in molecular orbital theory. Rev Mod Phys 1951;23:69–89. https://doi.org/10.1103/RevModPhys.23.69
[77] Gaussian 16, Revision C.01, Frisch M. J., Trucks G. W., Schlegel H. B. et al., Gaussian, Inc., Wallingford CT, 2016.
[78] Singh UC, Kollman PA. An approach to computing electrostatic charges for molecules. J Comput Chem 1984;5:129–45. https://doi.org/10.1002/jcc.540050204
[79] Becke AD. Density-functional thermochemistry. III. The role of exact exchange. J Chem Phys 1993;98:5648–52. https://doi.org/10.1063/1.464913
[80] Jorgensen WL, Chandrasekhar J, Madura JD, Impey RW, Klein ML. Comparison of simple potential functions for simulating liquid water. J Chem Phys 1983;79:926–35. https://doi.org/10.1063/1.445869
[81] Joung IS, Cheatham TE. Determination of alkali and halide monovalent ion parameters for use in explicitly solvated biomolecular simulations. J Phys Chem B 2008;112:9020–41. https://doi.org/10.1021/jp8001614
[82] Joung IS, Cheatham TE. Molecular dynamics simulations of the dynamic and energetic properties of alkali and halide ions using water-model-specific ion parameters. J Phys Chem B 2009;113:13279–90. https://doi.org/10.1021/jp902584c
[83] Abraham MJ, Murtola T, Schulz R, Páll S, Smith JC, Hess B, et al. GROMACS: high performance molecular simulations through multi-level parallelism from laptops to supercomputers. SoftwareX 2015;1–2:19–25. https://doi.org/10.1016/j.softx.2015.06.001
[84] Essmann U, Perera L, Berkowitz ML, Darden T, Lee H, Pedersen LG. A smooth particle mesh Ewald method. J Chem Phys 1995;103:8577–93. https://doi.org/10.1063/1.470117
[85] van Gunsteren WF, Berendsen HJC. A leap-frog algorithm for stochastic dynamics. Mol Simul 1988;1:173–85. https://doi.org/10.1080/08927028808080941
[86] Hess B, Bekker H, Berendsen HJC, Fraaije JGEM. LINCS: a linear constraint solver for molecular simulations. J Comput Chem 1997;18:1463–72. https://doi.org/10.1002/(SICI)1096-987X(199709)18:12<1463::AID-JCC4>3.0.CO;2-H
[87] Berendsen HJC, Postma JPM, van Gunsteren WF, DiNola A, Haak JR. Molecular dynamics with coupling to an external bath. J Chem Phys 1984;81:3684–90. https://doi.org/10.1063/1.448118
[88] Bussi G, Donadio D, Parrinello M. Canonical sampling through velocity rescaling. J Chem Phys 2007;126:014101. https://doi.org/10.1063/1.2408420
[89] Parrinello M, Rahman A. Polymorphic transitions in single crystals: a new molecular dynamics method. J Appl Phys 1981;52:7182–90. https://doi.org/10.1063/1.328693
[90] Nosé S, Klein ML. Constant pressure molecular dynamics for molecular systems. Mol Phys 1983;50:1055–76. https://doi.org/10.1080/00268978300102851
[91] Humphrey W, Dalke A, Schulten K. VMD: visual molecular dynamics. J Mol Graph 1996;14:33–8. https://doi.org/10.1016/0263-7855(96)00018-5
[92] The PyMOL Molecular Graphics System, Version 2.4.2 Schrödinger, LLC.
[93] Turner P. J. XMGRACE, Version 5.1.25. 2015.
[94] Jerabek-Willemsen M, Wienken CJ, Braun D, Baaske P, Duhr S. Molecular interaction studies using microscale thermophoresis. Assay Drug Dev Technol 2011;9:342–53. https://doi.org/10.1089/adt.2011.0380
[95] Magnez R, Thiroux B, Taront S, Segaoula Z, Quesnel B, Thuru X. PD-1/PD-L1 binding studies using microscale thermophoresis. Sci Rep 2017;7:17623. https://doi.org/10.1038/s41598-017-17963-1
[96] Cheng X, Veverka V, Radhakrishnan A, Waters LC, Muskett FW, Morgan SH, et al. Structure and interactions of the human programmed cell death 1 receptor. J Biol Chem 2013;288:11771–85. https://doi.org/10.1074/jbc.M112.448126
[97] Bailly C, Vergoten G. Flurbiprofen as a biphenyl scaffold for the design of small molecules binding to PD-L1 protein dimer. Biochem Pharm 2020;178:114042. https://doi.org/10.1016/j.bcp.2020.114042
[98] Ahmed M, Ganesan A, Barakat K. Leveraging structural and 2D-QSAR to investigate the role of functional group substitutions, conserved surface residues and desolvation in triggering the small molecule-induced dimerization of hPD-L1. BMC Chem 2022;16:49. https://doi.org/10.1186/s13065-022-00842-w
[99] Chen R, Yuan D, Ma J. Advances of biphenyl small-molecule inhibitors targeting PD-1/PD-L1 interaction in cancer immunotherapy. Future Med Chem 2022;14:97–113. https://doi.org/10.4155/fmc-2021-0256